H.1 Overview of the Inner Detector

H.1.1. Physics Goals

The task of the Inner Detector (ID) is to reconstruct the tracks and vertices with high efficiency, contributing, together with the calorimeter and muon systems, to the electron, photon, muon, jet recognition, missing transverse energy measurement, and supplying the important extra signature for short-lived particle decay vertices, such as b-quarks and strange particles. Many of the interesting physics questions at the LHC require high luminosity, and so the primary goal is to operate at a luminosity of 10^{34} cm^{-2}s^{-1}. Emphasis is also put on the performance necessary for the physics accessible during the initial lower luminosity running (a few times 10^{33} cm^{-2}s^{-1}), using more complex signatures such as τ-lepton detection and heavy-flavour tags from secondary vertices. Finally, the detector is conceived for assured performance even at the highest possible luminosities (in excess of 10^{34} cm^{-2}s^{-1}) which ultimately could be delivered by the LHC.

H.1.2. The Inner Detector Layout

A cross-sectional view of one quarter of the inner detector (ID) is given in Figure H.1 . It combines high-resolution detectors at inner radii with continuous tracking elements at outer radii, all contained in a solenoidal magnet with a central field of 2T.

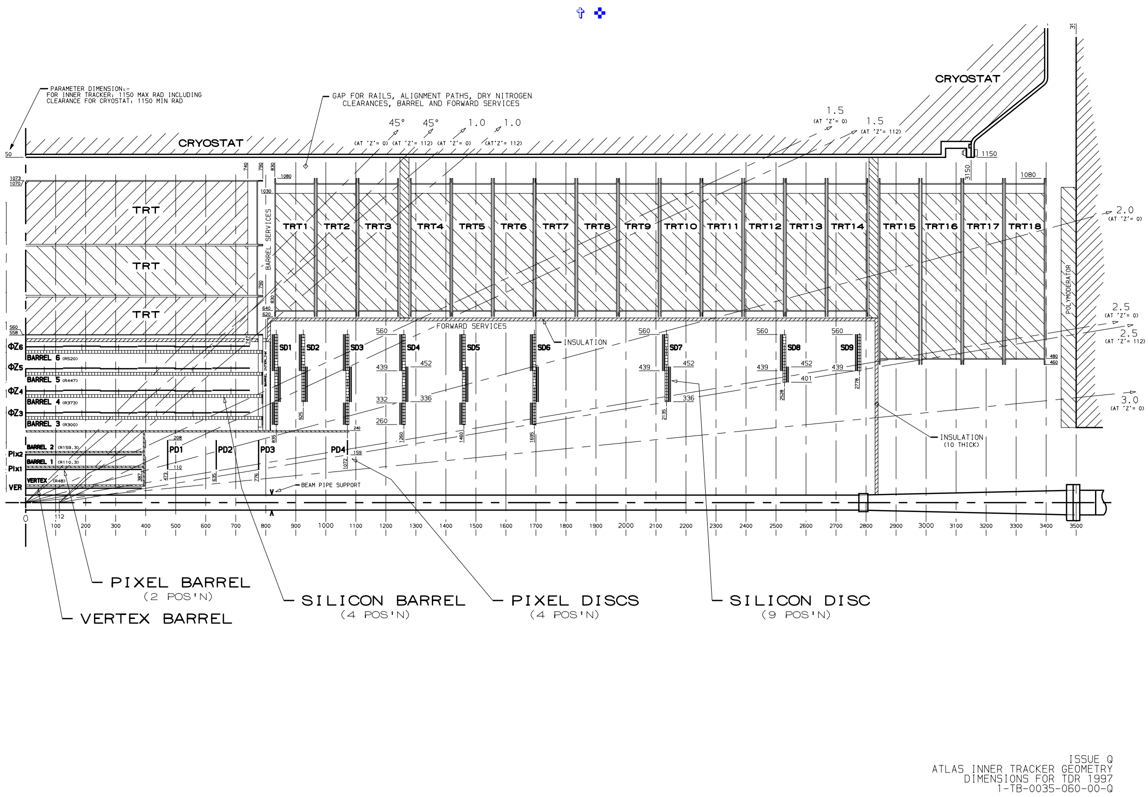

Figure H.1 A cross-section of the ID engineering layout through the beam axis.

The momentum and vertex resolution targets require high-precision measurements to be made with fine-granularity detectors given the very large track density expected at the LHC. Semi-

Table H.1 Parameters of the Inner Detector. The resolutions quoted are typical values (the actual resolution in each detector depends on $|\eta|$).

System	Position	Area (m^2)	Resolution σ (μm)	Channels (10^6)	η coverage
Pixels	1 removable barrel layer	0.2	$R\phi = 12$, $z = 66$	16	±2.5
	2 barrel layers	1.4	$R\phi = 12$, $z = 66$	81	±1.7
	4 end-cap disks on each side	0.7	$R\phi = 12$, $R = 77$	43	1.7-2.5
Silicon strips	4 barrel layers	34.4	$R\phi = 16$, $z = 580$	3.2	±1.4
	9 end-cap wheels on each side	26.7	$R\phi = 16$, $R = 580$	3.0	1.4–2.5
TRT	Axial barrel straws		170 (per straw)	0.1	±0.7
	Radial end-cap straws		170 (per straw)	0.32	0.7–2.5
	36 straws per track				

conductor tracking (SCT) detectors, using silicon microstrip and pixel technology offer these features. Highest granularity around the vertex region is achieved using semiconductor pixel detectors. However, the total number of precision layers must be limited because of the material they introduce, and because of their high cost. At least four strip layers and three pixel layers are therefore crossed by each track in this design.

A large number of tracking points (typically 36 per track) is given by a straw tube tracker (TRT) which provides the possibility of continuous track-following with much less material per point and at lower cost. The straw hits at the outer radius contribute to the momentum measurement, with the lower precision per point compared to the silicon being compensated by the large number of measurements and the higher average radius. The high density of measurements in the outer part of the tracker is also valuable for the detection of V^0 decays, which form a crucial part of the signature for CP violation in the B system. In addition, the electron identification capabilities of the whole experiment are enhanced by the detection of transition-radiation photons in the straw tubes.

The combination of the semiconductor and straw-tube/transition-radiation techniques gives very robust pattern recognition and high precision in both ϕ and z coordinates. The relative precisions of the different measurements are well matched, so that no single measurement dominates the momentum resolution. This means that the overall performance is robust, even in the event that a single system does not perform to its full specification.

The outer radius of the tracker cavity is 115 cm, fixed by the inner dimension of the cryostat containing the liquid argon EM calorimeter, and the total length is 7 m, limited by the position of the end-cap calorimetry. Mechanically, the Inner Detector consists of three units: a barrel part extending over ±80 cm, and two identical end-caps covering the rest of the cylindrical cavity. The precision tracking elements are contained within a radius of 56 cm, followed by the continuous tracking, and finally the general support and service area at the outermost radius. In order to give uniform coverage over the full acceptance, the final TRT wheels at high z must extend inwards to a lower radius than the rest of that detector.

In the barrel, the high-precision detector layers are arranged on concentric cylinders around the beam axis in the region with $|\eta| < 1$, while the end-cap detectors are mounted on disks perpendicular to the beam axis. The pixel layers are segmented in $R\phi$ and z, while the silicon strips use small angle (40 mrad) stereo to measure both coordinates, with one set of strips in each layer measuring ϕ. The barrel TRT straws are parallel to the beam direction.

All the end-cap tracking elements are located in planes perpendicular to the beam axis. The strip detectors have one set of strips running in radial directions, and a set of stereo strips at an angle of 40 mrad. The continuous tracking consists of radial straws arranged into wheels.

The basic design parameters and the resolutions for space-point measurements are summarised in Table H.1 . The layout provides full tracking coverage over $|\eta| \leq 2.5$, including impact parameter measurements and vertexing for heavy-flavour and τ tagging. The secondary vertex measurement performance will be enhanced with an innermost additional layer of pixels, at a radius of about 4 cm, as close as is practical around the beam pipe. A large amount of interesting physics can be done with this detector during the initial lower luminosity running, especially in the B sector, but recent physics studies have demonstrated the value of good b-tagging performance during all phases of the LHC, for example in Higgs and supersymmetry searches. It is therefore considered as an option that the B-layer can be replaced to give the highest possible performance throughout the Inner Detector lifetime. The exact lifetime of the layer will depend on the time taken to accumulate integrated luminosity, but using a realistic model, the earliest date for such a replacement is around 4 years after commission.

Evolution of the Layout

Although the baseline tracker concept had the same complementary sub-systems of pixels, precision hits and TRT continuous tracking as presented above, the technology for the precision hits in the forward region was evolved from micro-strip gas chambers (MSGCs) to silicon strip detectors. In the inner-most forward region, silicon strip detectors were also chosen over GaAs strip detectors since studies showed that damage from charged particles was significant for GaAs detectors. For these reasons, the latest design consists of a unified silicon strip detector in the intermediate radial range between the pixel detector and the TRT.

H.1.3. Summary of Performance

H.1.3.1 Single track performance

Figure H.2 shows an example of the use of the ID in the search for the Higgs boson. The decay $H \rightarrow ZZ^* \rightarrow e^+e^-\mu^+\mu^-$ was simulated together with the expected pile-up at the LHC design luminosity, for a Higgs mass (m_H) of 130 GeV.

A search was performed for all tracks with transverse momenta above 5 GeV. In spite of the occupancy created by looping tracks and hits from secondary interactions, the pattern recognition successfully identified the four high-p_T lepton tracks. The reconstructed tracks are plotted in red. No false tracks were found.

The muon tracks can be identified using the toroid spectrometer, while the electron tracks can be identified using energy-momentum matching with the EM calorimeter. In addition, the transition-radiation performance is illustrated in this event. The e^- track has nine hits with energies above the transition-radiation discriminator threshold (plotted in red), while the neighbouring

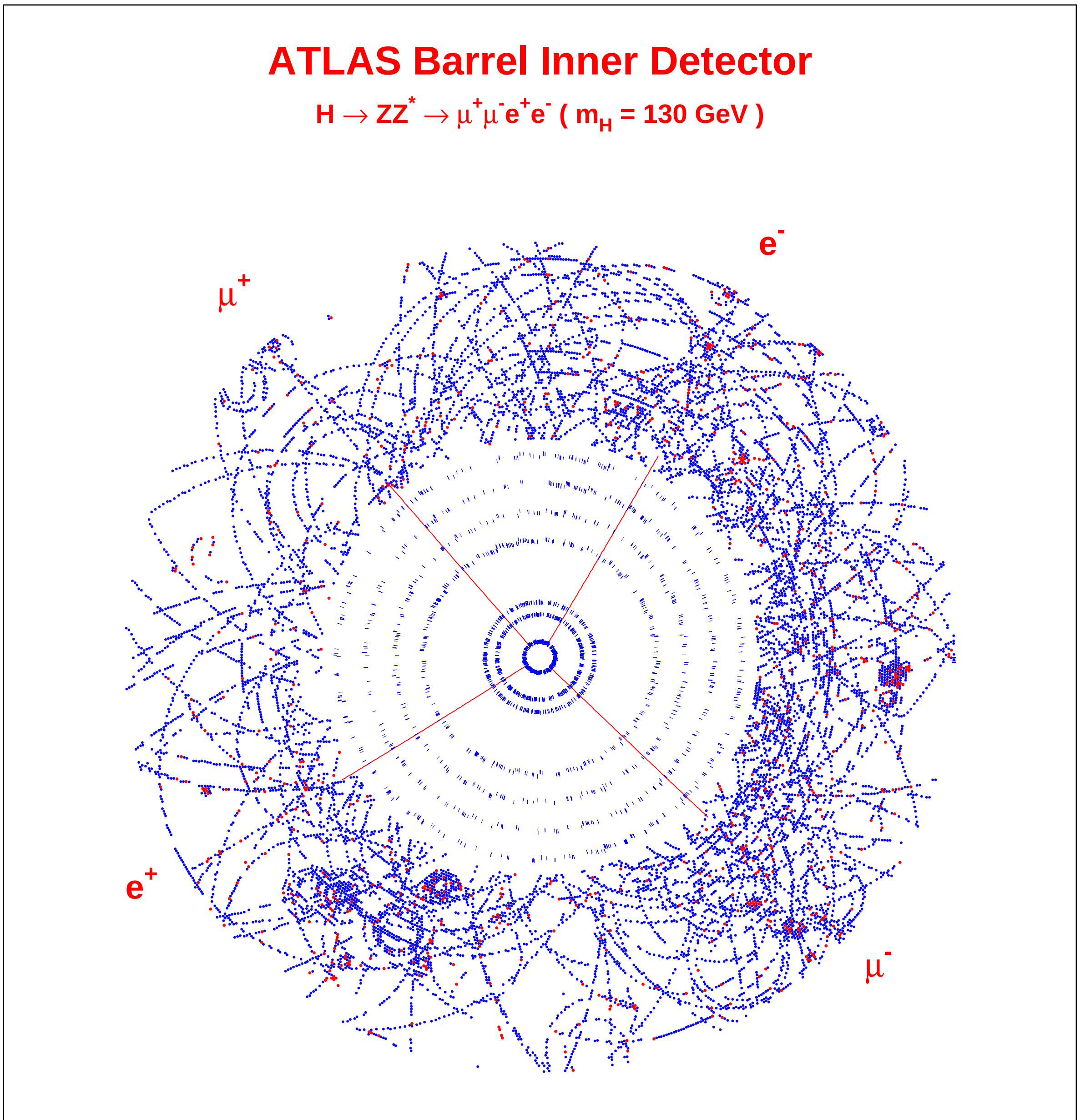

Figure H.2 Event display of the process $H \rightarrow \mu^+\mu^-e^+e^-$ in the barrel part of the inner detector

μ^+ has only two such hits. This additional signature enhances the overall electron identification performance.

In Figure H.3 the number of silicon elements traversed is plotted, giving one hit for each pixel layer (in this case including the B-layer), and two for each strip layer (Rϕ and stereo measurement). Hence the nominal seven space points are made up of eleven measurements, in three pixel layers and four SCT layers. In Figure H.4 the number of crossed straws in the TRT is plotted. In the end-cap TRT, a lower number of straws is used in some wheels in order to minimise the material and give the required number of hits without increased cost.

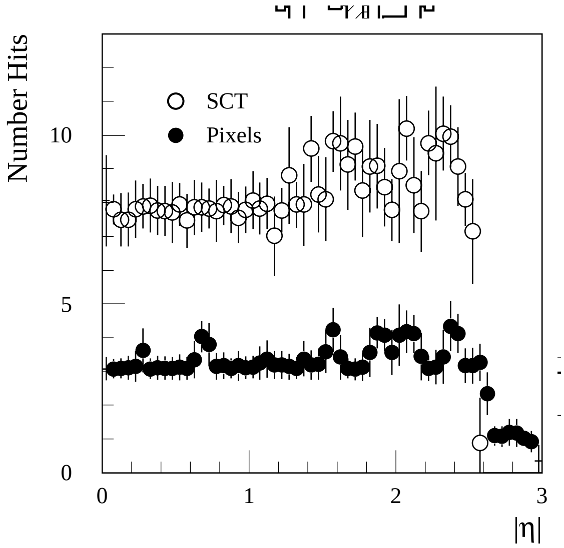

Figure H.3 Number of hits per track in the precision detectors.

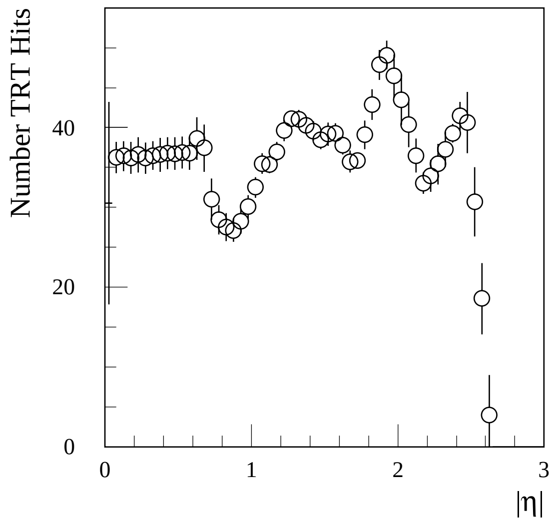

Figure H.4 Number of hits per track in the TRT.

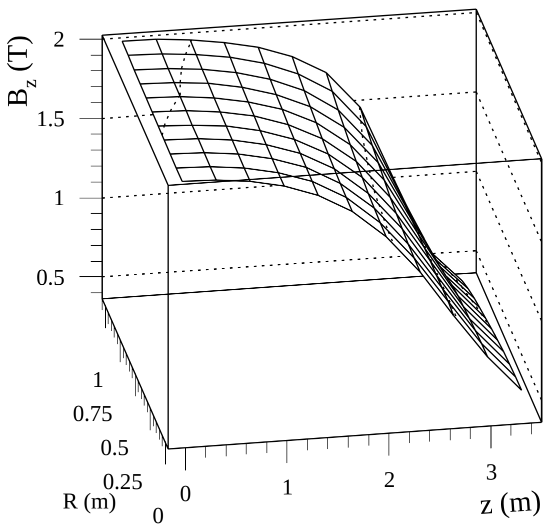

Figure H.5 The magnetic field strength in the beam direction as a function of R and z.

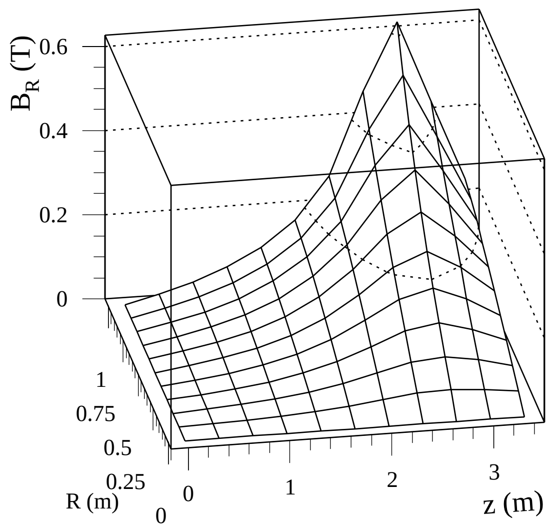

Figure H.6 The radial component of the magnetic field as a function of R and z.

The full momentum resolution, combining the information from the discrete precision points and the large number of drift-time measurements of the TRT in a global fit through the realistic solenoid field map (Figure H.5 and Figure H.6), is shown in Figure H.7 . This resolution is sufficient to identify the charge sign of particles up to the highest energies expected at LHC, for example from the decays of new vector bosons in the TeV mass range, allowing the parity violating asymmetries to be investigated.

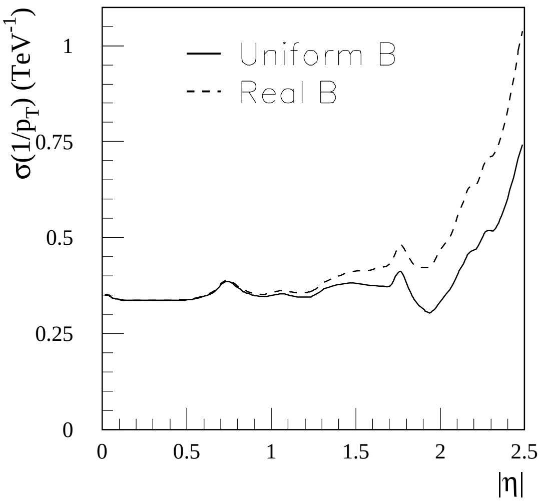

Figure H.7 The Inner Detector momentum resolution with beam constraint, for tracks with p_T = 500 GeV, for the real solenoidal field compared to a uniform 2T field.

A crucial parameter for the physics performance of the ID is the resolution on the impact parameters of tracks from secondary vertices. The impact parameter resolution can be parametrised in $R\phi$ as $\sigma(d_0) = 11 \oplus 60 / p_T \sqrt{\sin\theta}$ and in z as $\sigma(z_0) = 70 \oplus 100 / p_T \sqrt{\sin^3\theta}$ (in μm), with the existence of dedicated B-physics layer of pixels at 4 cm radius. The full simulation of this performance for different track transverse momenta is shown in Figure H.8 and Figure H.9 . During the initial low luminosity running, B-physics studies will concentrate on

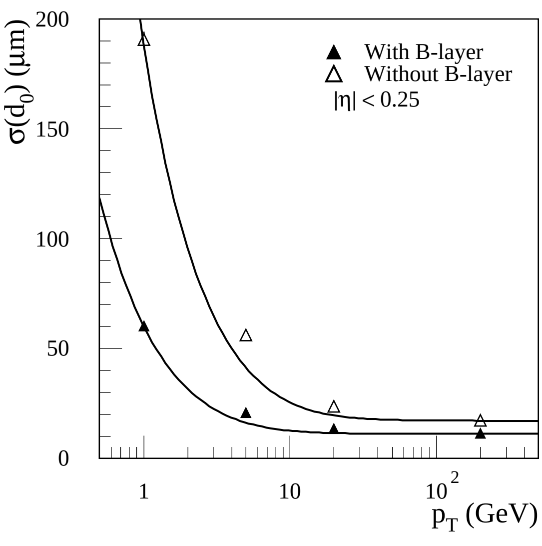

Figure H.8 Transverse impact parameter resolution as a function of p_T for η=0.

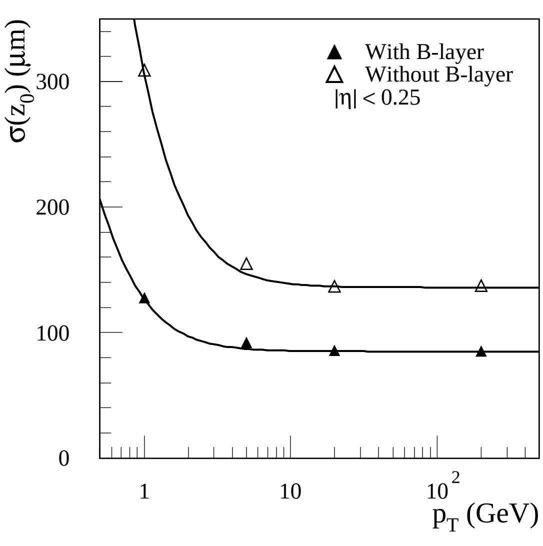

Figure H.9 Longitudinal impact parameter resolution as a function of p_T for η=0.

CP-violating channels in the B-system. In addition, the ability to tag jets containing b-quarks will be used in Higgs and supersymmetry searches up to the highest luminosities.

The ID has excellent pattern recognition properties, with an efficiency of above 99% for finding muons with p_T = 20 GeV, even in the presence of the pile-up expected at design luminosity. Tracks have also been studied in jets, for example from $H \rightarrow b\bar{b}$ with m_H = 400 GeV. An efficiency of ~ 90% can be obtained for tracks with p_T > 1 GeV, with cuts which ensure that the fraction of fake tracks anywhere in the acceptance remains below ~ 0.5%.

H.1.4. Material Budget

The precision layers based on silicon semiconductor technology and the TRT have a significant amount of material in the tracking volume, from the element itself, associated electronics, and its services, such as power cabling, cooling and monitoring cabling. In addition, the high momenta of the tracks necessitate a very high level of precision in the detector, and so the support structure requires mechanical stability at the level of a few tens of microns over distances of metres. This requirement can only be met by a rigid structure which inevitably increases the material budget. The distribution of material, in radiation lengths, as a function of $|\eta|$ is shown in Figure H.10 . The level corresponds to an average of 43% X_0 with a peak at ~ 60%. The effect of the material can be clearly identified in the ATLAS performance, but it does not create unacceptable problems for physics studies. Most of these studies have been performed including the dedicated B-layer.

For example, photons can convert inside the ID, and so reduce the signal for the channel $H\rightarrow\gamma\gamma$ by creating tails in the energy measurement. Careful studies, using the ID to reconstruct conversions wherever possible, show that the material causes an additional loss of 3.8% of the signal outside of a mass bin of $\pm$ 1.4 σ centred on the peak. Since 80% of the signal remains inside the bin, this loss is considered to be tolerable. 85% of converted photons with high p_T are reconstructed by the ID. Those photons which are not reconstructed have mostly converted at large radius, and their energies are therefore still well measured in the calorimeter.

The material has a similar effect on electrons, provoking bremsstrahlung and affecting both the energy measurement in the calorimeter and the track momentum measurement, and hence the energy-momentum matching used for electron identification. An example of this effect was studied in for the channel $H \rightarrow eeee$, with a Higgs mass of 130 GeV. The overall reconstruction efficiency was 89%, but only 85% of the events lie within $\pm 2\sigma$ of the mass peak. The tails in the mass distribution are increased by the effect of the ID material, with the material at small radius having the largest impact, but once again the effect on the physics reach is tolerable.

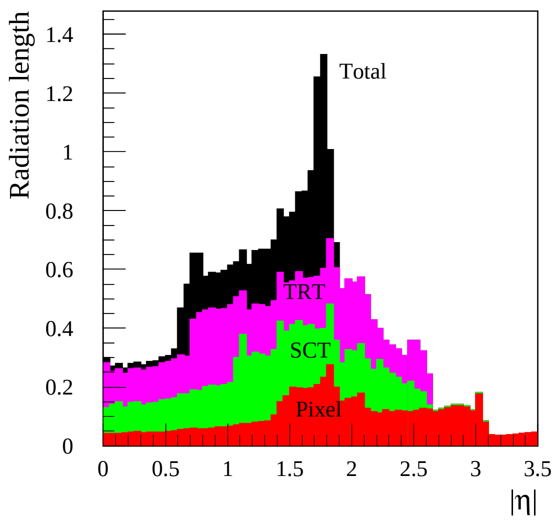

Figure H.10 The amount of material in radiation lengths in the Inner Detector, including the B-layer as a function of η. The successive curves show the cumulative material in the pixel, SCT and TRT active volumes. The final curve includes the material associated with the Inner Detector, mainly due to services, which is outside the sensitive tracking volume but inside the electromagnetic calorimeter cryostat.

Because low-Z materials are used, the ratio of interaction length to radiation length is relatively high. This causes a loss of efficiency for hadrons, especially at low momentum, and scattering also degrades the impact parameter resolution. The efficiency for reconstructing pions with 1 GeV of p_T falls as low as 87% in the worst region. After cuts, within b-jets, 31% of the tails in the impact parameter distribution are due to interactions in the material of the detector, mostly from photon conversions, but also from nuclear interactions. In spite of this, a rejection of 80 is obtained against light quark jets and 40 against gluon jets, while retaining an efficiency for tagging b jets of 50%, which is sufficient to maintain the good physics performance.

Work is in progress to attempt to reduce the material budget still further, by detailed optimisation of the active detectors, and by further integration of the overall support structure.

H.2 Inner Detector Schedule

H.2.5. Overall Schedule and Milestones

Figure H.11 shows the overall schedule for the inner detector. In order for the detector to be ready for full operation in mid-2005, the detector installation inside the liquid argon cryostat of the EM calorimeter must begin in the second quarter of 2004, with cabling complete by the fourth quarter of 2004, leaving nine months for final testing and commissioning. Given the complexity of the detector, a six-month period has also been foreseen before installation begins, during which time the fully assembled detector will be tested in the surface assembly area. This

Figure H.11 The overall ID construction schedule.

procedure should minimise the risk of delays in the final testing phase, when access to the detector will be restricted and the working environment in the pit will be difficult. All the ele-

Table H.2 List of milestones of the ID construction.

Milestone	Date
Begin testing complete ID on surface	September 2003
Start installation into ATLAS	March 2004
Begin commissioning	September 2004
First physics	July 2005

ments of the ID must therefore be assembled by the fourth quarter of 2003. This constrains the construction schedule of the sub-systems.

H.3 Semiconductor Tracker (SCT)

H.3.1. Layout

The SCT system is designed to provide four precision measurements per track in the intermediate radial range, contributing to the measurement of momentum, impact parameter and vertex position, as well as providing good pattern recognition by the use of silicon microstrip detector. The system is an order of magnitude larger in surface area than previous generations of silicon microstrip detectors, and in addition must face radiation levels which will alter the fundamental characteristics of the silicon wafers themselves.

Requirements for the full inner detector translate in the case of the SCT as follows:

- The $(\delta p_T / p_T) < 0.3$ requirement at $p_T = 500$ GeV with a beam constraint imposes an r-ϕ measurement accuracy of ~ 20 μm at the SCT radius. The requirement to separate multiple vertices within a bunch crossing imposes an accuracy on the z-measurement of < 1mm in the SCT. That constraint is made more stringent by requirements of K^0 reconstruction and mass resolution where a z-measurement of ~ 0.5 mm is required in the SCT.
- The requirement of 2-track resolution <200 μm at R=30 cm, in order to keep track losses in b-jets to <5%, also imposes a constraint on the r-ϕ readout pitch.

To satisfy these criteria, the SCT design assumes the geometrical configuration described in the overview of the inner detector. The requirements lead to a silicon microstrip detectors with 80 μm pitch and a small stereo measurement of 40 mrad. The detailed parameters of the layout are given in Table H.3 and Table H.4 . The layout consists of 4 central barrel layers in the radial range 30 < R < 52 cm, and 9 disks in each of the forward and backward directions in the radial range 26 < R < 56 cm.

H.3.2. Radiation Environment

The radiation levels in the Inner Detector cavity will be extremely high, leading to damage in both the silicon detectors and the electronics. The most relevant quantity for the damage in silicon detectors is the fluence expressed in terms of 1 MeV equivalent neutrons. This is shown in Figure H.12 . The level of radiation is affected by the exact materials in the system. In the case

Table H.3 Barrel Silicon Strip Characteristics.

Radius (mm)	1/2 length (mm)	Tilt angle (degrees)	Pitch (μm)	# modules	# channels	Total area (m^2)	Orientation
300.0	746.7	10.0	80.0	12 x 32	589824	2 x 3.13	Φ,u (40 mr)
373.0	746.7	10.0	80.0	12 x 40	737280	2 x 3.91	Φ,v
447.0	746.7	10.0	80.0	12 x 48	884736	2 x 4.70	Φ,u
520.0	746.7	10.0	80.0	12 x 56	1032192	2 x 5.48	Φ,v

Total modules: 2112

Total substrate area: 2 x 17.2 = 34.4 m^2

Estimated Power (detector+ electronics+ services): ~13 kW

Total channels 3,244,032

Modules are staggered in radius by $\pm$1 mm to give overlap in z, and an overlap of 1% in ϕ makes the detector hermetic for p_T > 1 GeV/c. A dead space does remain between daisy-chained detectors.

Table H.4 Forward Silicon Strip Characteristics

#	z (mm)	Radius (inner/outer) (mm)	Modules (I/M/O)	Channels	Total Area (m^2) (external)	Orientation
1	835.0	259-560	40 / 40 / 52	4*101376	4*0.8580	Φ,u (40 mrad)
2	925.0	336-560	- / 40 / 52	4*70656	4*0.7109	Φ,v (40 mrad)
3	1072.0	259-560	40 / 40 / 52	4*101376	4*0.8580	Φ,u
4	1260.0	259-560	40 / 40 / 52	4*101376	4*0.8580	Φ,v
5	1460.0	259-560	40 / 40 / 52	4*101376	4*0.8580	Φ,u
6	1695.0	259-560	40 / 40 / 52	4*101376	4*0.8580	Φ,v
7	2135.0	336-560	- / 40 / 52	4*70656	4*0.7109	Φ,u
8	2528.0	401-560	- / 40 / 52	4*70656	4*0.55715	Φ,v
9	2788.0	440-560	- / - / 52	4*39936	4*0.40405	Φ,u

Total Modules: 1976

Total substrate area 26.692 m^2 (including edges)

Estimated power (detectors + electronics + services): ~12 kW

Total channels: 3035136

A z-stagger of 0.5cm allows overlaps.

Pitch in μm (min/max):

Inner	**54.53/69.43**
Middle	**70.48/94.74**
Outer	**70.92/90.34**

of the Inner Detector, the presence of the TRT radiator and specially installed polythene disks on the end-cap calorimeters reduces the energy of neutrons in the cavity and helps to reduce the damage they cause.

The dominant source of radiation at small radius comes from direct pp interactions. At a luminosity of 10^{34} $cm^{-2}s^{-1}$, typically 23 interactions occur per bunch crossing. The particles are produced approximately uniformly in rapidity, and with low p_T. Given the 2 Tesla solenoidal field of ATLAS, these low p_T particles (‘loopers’) traverse multiple SCT layers. Other charged radiation will result from subsequent material effects (photon conversions, nuclear interactions).

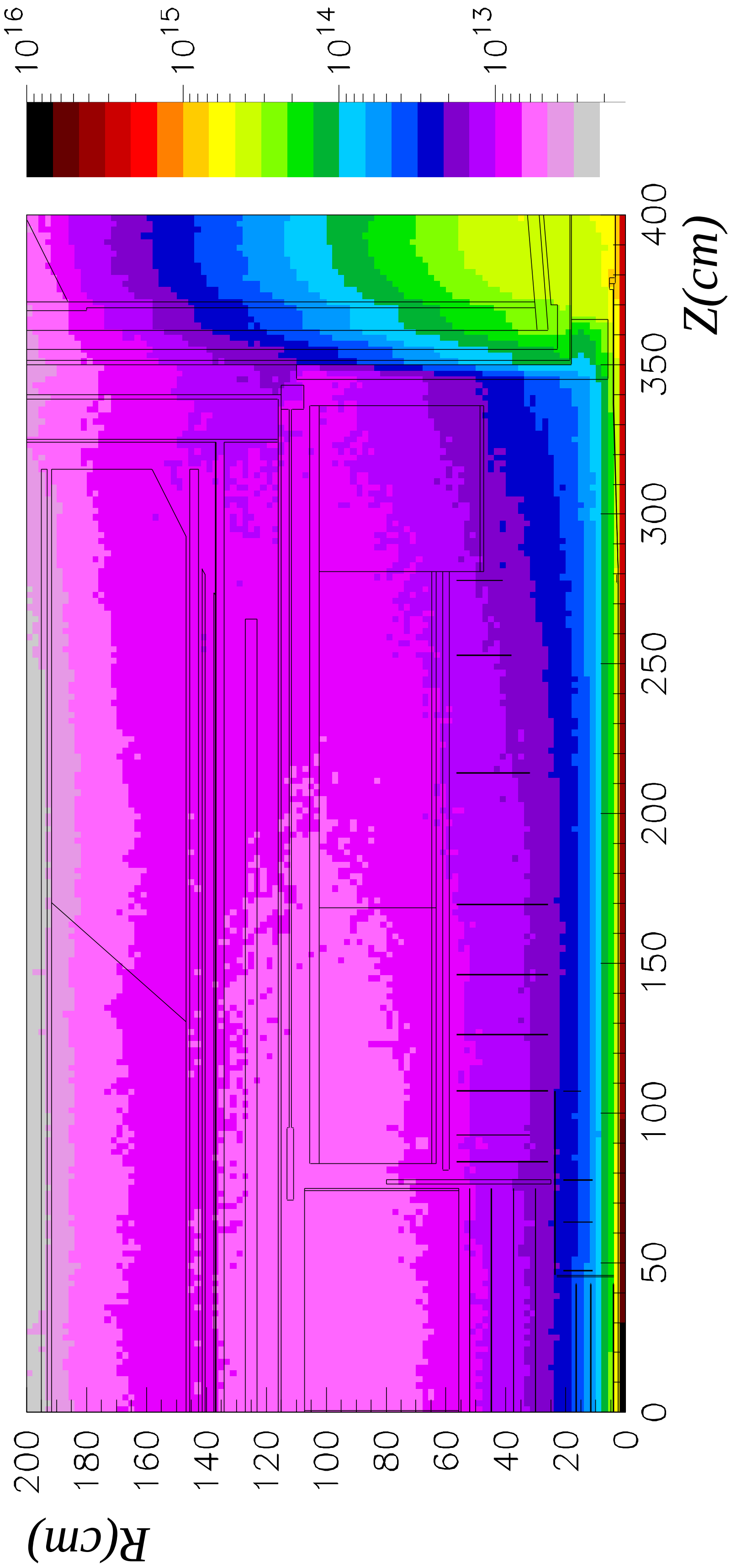

Figure H.12 Annual fluence in the ID cavity in units of 1 MeV equivalent neutrons per cm^2 per year.

Beam losses and beam-gas interactions contribute an order of magnitude less radiation than direct interactions at high luminosity. The charged particles are predominantly pions. Because of interactions in the calorimeter, albedo neutrons are also a significant source of radiation, being dominant at larger radii in the SCT.

Figure H.13 shows the distribution of interactions per bunch crossing at a luminosity of $10^{34}\ cm^{-2}s^{-1}$. Figure H.14 shows the distribution in η of the produced particles, obtained using both the PYTHIA [8-21] and DTUJET [8-22] event generators.

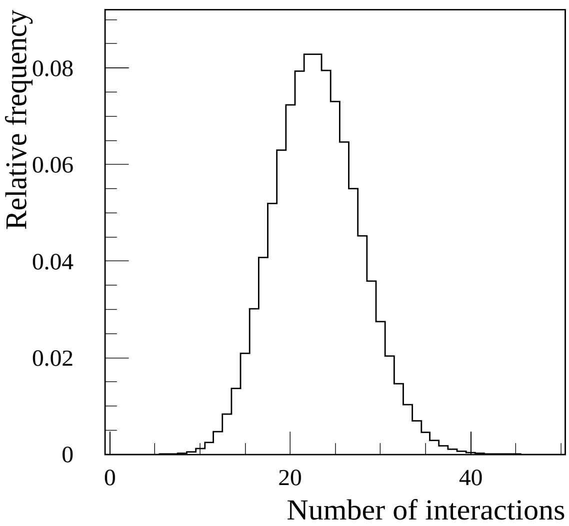

Figure H.13 Distribution of the number of interactions per bunch crossing at a luminosity of $10^{34}cm^{-2}s^{-1}$.

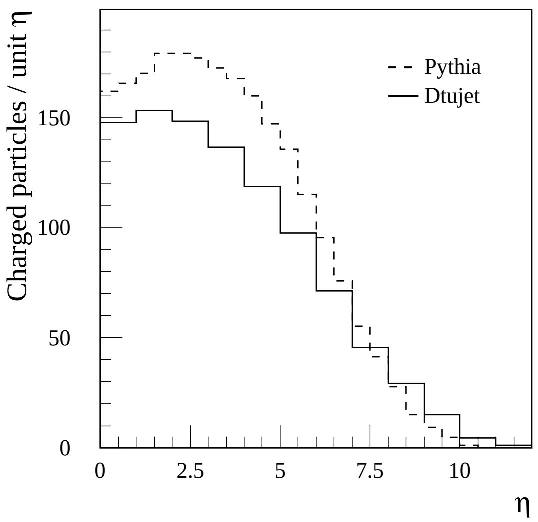

Figure H.14 Distribution in η of charged particles produced per bunch crossing at a luminosity of $10^{34}cm^{-2}s^{-1}$. Results are shown for both the DTUJET and PYTHIA minimum bias event generators.

The procedure used to evaluate the fluence is to assume 3 years of low-luminosity operation ($10^{33}\ cm^{-2}s^{-1}$ for 10^7 s/yr) followed by 7 years of high-luminosity operation ($10^{34}\ cm^{-2}s^{-1}$ for 10^7 s/yr). A proton-proton inelastic (non single diffractive) cross-section of $\sigma_{pp} = 70$ mbarn is assumed. The DTUJET code has been used to generate minimum bias particles, and the FLUKA transport code has been used to transport the produced particles, and treat their subsequent decays or interactions. An uncertainty of ± 50 % is nominally assigned to these fluences due to the combined uncertainties of the inelastic cross-section and the event multiplicity. Also included in this estimate are radiation damage corrections described below. It is noted that the generator discrepancy is within this uncertainty, with DTUJET on the low side.

Within FLUKA, a detector model has been constructed by Ferrari, which reproduces the location and quantity of material in the Inner Detector and Calorimeter regions. In particular, beam-pipe supports and flanges, the detector supports and services, the forward neutron moderator and the integrated forward calorimeter are modelled. Since the bulk radiation damage to silicon dominantly results from the non-ionising inelastic cross-section (NIEL), it is convenient to normalise the fluences to a fixed energy and particle type, historically 1 MeV neutrons. The most recent NIEL neutron damage normalisation functions [8-23] have been used in this evaluation, together with the charged particle normalisation functions of Huhtinen et al. The total neutral and charged particle fluence, normalised to the 1 MeV equivalent neutron fluence, is shown in Figure H.12 . The results are averaged over ϕ. The fluences appropriate to each SCT detector element are listed in Table H.5 and Table H.6 . Although the neutron fluences have been evaluated to low energy, only neutrons with energy >100 keV are used in the damage calculations, since the damage cross-section drops significantly at lower energies.

Table H.5 Estimated barrel annual fluence after normalization to the damage of 1 MeV neutrons, at a luminosity L=10^{34} $cm^{-2}s^{-1}$. The occupancy is estimated using the PYTHIA generator, and DTUJET is used to evaluate the fluence. The fluence has an estimated uncertainty of ± 50 %.The typical point-to-point statistical uncertainty of $\pm(5-10)$ % is not listed.

	Fluence (neutral) x 10^{12} n_{eq}/cm^2		**Total Hadron Fluence (10^{12} n_{eq}/cm^2)**		**Total Hadron Fluence after 10 yrs (10^{14} n_{eq}/cm^2)**	
	z=0 cm	**z=75 cm**	**z=0 cm**	**z=75 cm**	**z=75cm**	**Design value**
Barrel 1	8.9	9.2	17.5	17.8	1.30	1.95
Barrel 2	7.4	8.1	13.4	14.1	1.03	
Barrel 3	7.3	7.1	11.7	11.6	0.85	
Barrel 4	6.4	7.0	9.8	10.5	0.77	

H.3.3 Occupancy in SCT modules

Although the accumulated radiation level is high, it is extremely rare to find events where modules have occupancies above 10% due to its fine granularity at a time. Figure H.15 and Figure H.16 show the mean number of hits per module (note, an area of 128 mm x 63.6 mm and not per strip) as a function of $|\eta|$ for different SCT layers, and the results, averaged over η are summarised in Table H.7 . For the pile-up events, the occupancy scales with the area (in $\eta-\phi$) subtended by the module. For b-jets, the occupancy is nearly independent of radius since the size of the jet in $\eta-\phi$ is smaller than the area of a module. In both cases, the mean occupancies are low, a feature that simplifies the pattern recognition.

H.4 Detectors

H.4.4. Radiation damages

The problem of radiation damage to silicon detectors has been the subject of a large R&D programme, and it is now possible to describe the behaviour of the detectors in some detail up to fluences of 10^{15} 1 MeV equivalent neutrons per cm^2. The depletion voltage rises with increasing fluence, and the operation of the detectors is limited by the maximum voltage to be sustained. The leakage current also rises with increasing fluence, and the operation of detectors is limited by the thermal runaway of the detector, which is a critical issue in designing the SCT modules.

The effect of radiation damage is strongly temperature dependent, with both beneficial annealing effects in the depletion voltage and the leakage current, in which the damage is recovered with time, and also “reverse annealing” which leads to an increase in the depletion voltage with time. The reverse annealing effect can be suppressed if the detector is operated at low tempera-

Table H.6 Estimated SCT annual fluence after normalizing to the damage of 1 MeV neutrons, at a luminosity L=10^{34} $cm^{-2}s^{-1}$. DTUJET is used to evaluate the fluence. The fluence has an estimated uncertainty of ± 50 %. The typical point-to-point statistical uncertainty of $\pm(5-10)$ % is not listed.

		Max Neutral Fluence (10^{12} n_{eq}/cm^2)	Total Hadron Fluence (10^{12} n_{eq}/cm^2)	Total Hadron Fluence after 10 yrs (10^{14} n_{eq}/cm^2)	Design value after 10 yrs (10^{14} n_{eq}/cm^2)
Disk 1	Module 1	9.2	19.6	1.43	2.14
	Module 2	9.8	16.9	1.23	1.94
	Module 3	8.4	12.5	0.91	1.86
Disk 2	Module 2	7.9	15.2	1.11	
	Module 3	7.4	11.6	0.85	
Disk 3	Module 1	8.8	18.6	1.36	
	Module 2	8.0	15.0	1.10	
	Module 3	7.0	11.3	0.82	
Disk 4	Module 1	7.8	17.7	1.29	
	Module 2	8.3	15.6	1.14	
	Module 3	6.9	11.2	0.82	
Disk 5	Module 1	8.6	18.4	1.34	
	Module 2	8.7	15.7	1.15	
	Module 3	7.8	12.1	0.88	
Disk 6	Module 1	9.0	19.0	1.39	
	Module 2	8.1	15.4	1.12	
	Module 3	7.6	12.0	0.88	
Disk 7	Module 2	9.1	16.5	1.20	
	Module 3	8.7	13.2	0.96	
Disk 8	Module 2	10.7	16.8	1.23	
	Module 3	10.6	15.2	1.11	
Disk 9	Module 3	12.2	17.0	1.24	

Table H.7 Average number of hits per module and occupancies for SCT layers.

	Pile-up		b-jets	
	Num hits	**Occupancy**	**Num hits**	**Occupancy**
Barrel 1	4.7	6.1×10^{-3}	13	1.7×10^{-2}
Barrel 2	3.8	4.9×10^{-3}	12	1.6×10^{-2}
Barrel 3	3.1	4.0×10^{-3}	11	1.4×10^{-2}
Barrel 4	2.6	3.4×10^{-3}	11	1.4×10^{-2}

ture: -5 to -10°C (-7°C average in the SCT). This operating temperature also has the beneficial effect of reducing the leakage current and hence heat generation inside the detector substrate.

From detector studies after irradiation, a model has been developed for the evolution of depletion voltage V_D, bulk leakage current I_L, and charge collection efficiency ε_{eff} as a function of the radiation fluence Φ, the radiation rate $d\Phi/dt$, the radiation type, and the operational temperature T of the detector [8-24].

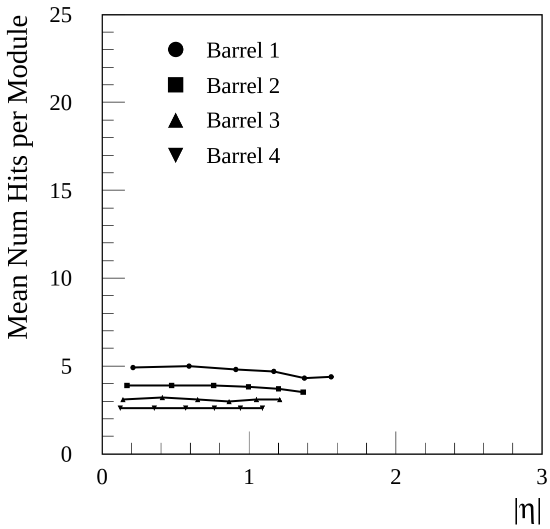

Figure H.15 Mean number of hits per SCT module for pile-up.

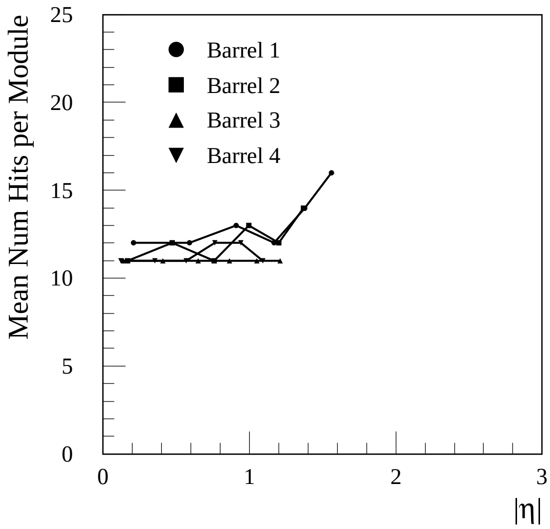

Figure H.16 Mean number of hits per SCT module for b-jets.

Figure H.17 shows the development of V_D as a function of time, assuming an operational temperature of -7 °C, and assuming several access and warm-up scenarios, at an integrated fluence close to the maximum expected for the SCT. A detector thickness of 300 µm is assumed. Assuming conservatively that the detector is removed each year for maintenance, a 'standard access procedure' (SAP), a warm-up time of 2 days at 20 °C, and a 14 day maintenance period at 17 °C, has been defined. The effect of different operating temperatures, assuming SAP, is shown for the range of expected V_D in Figure H.18 .

Table H.8 and Table H.9 list the projected V_D for module operation at extreme positions of each barrel layer and forward disks, respectively, assuming the fluences discussed in Table H.5 and Table H.6 . Figure H.19 shows the depletion voltages of the upper bound of the systematic uncertainty at various locations summarized in the Table H.5 and Table H.6 .

The maximum detector leakage currents at an operating temperature of -7 °C and the SAP access scenario is listed in Table H.10 . In no case the bulk detector current for a module will exceed 2 mA. Also shown in Table H.10 is the predicted charge collection efficiency ε_{COLL} for each module type. At operating voltages not exceeding 350 V, ε_{COLL} remains adequate.

H.4.5. Technology Choice

The parameters described in the specifications have evolved from prototyping studies within ATLAS, in the DRDC collaborations RD2 and RD20, and from the SSC. Prototyping has involved Micron Semiconductor, Hamamatsu, CSEM, Sintef, MPI and MSU. Results with detectors from these manufacturers have influenced the final designs.

After long collaborative work in the SCT community in the comparison of two technologies: p-readout (p-in-n) and n-readout (n-in-n) in the n-bulk silicon, the following results were established:

1) It is confirmed that p-in-n detectors have to be run close to the full depletion voltage with binary electronics post-irradiation for full efficiency.

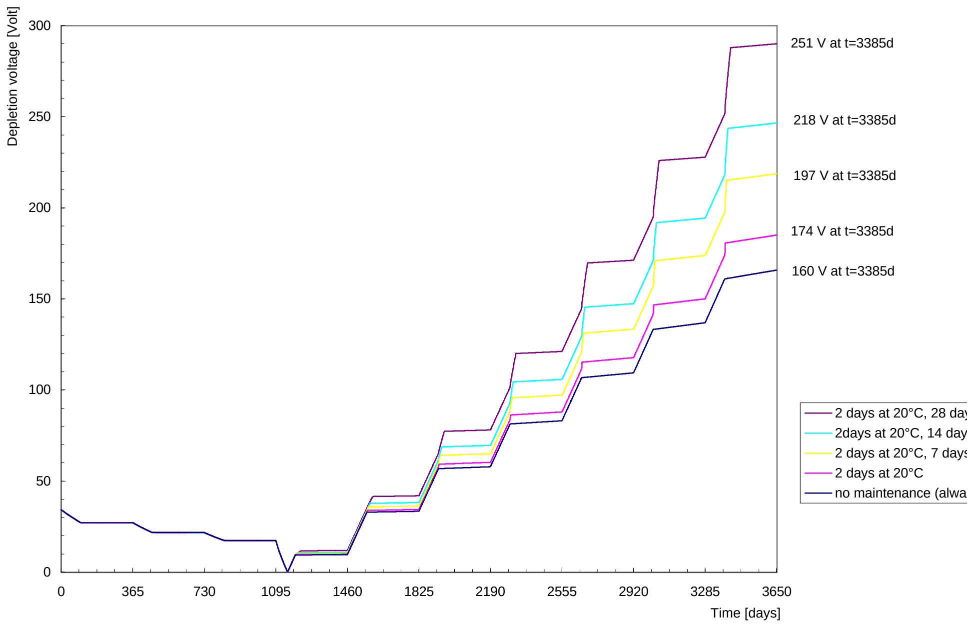

Figure H.17 Dependence of detector depletion voltage V_D as a function of time, assuming an integrated fluence after 10 years of 1.4 x 10^{14} n_{eq}/cm^2, and an operating temperature of -7 °C. Different access scenarios are assumed as annotated. The standard access procedure assumed for the SCT design is an annual warm-up of 2 days at 20 °C, and 14 days at 17 °C. The detector thickness is assumed to be 300 µm.

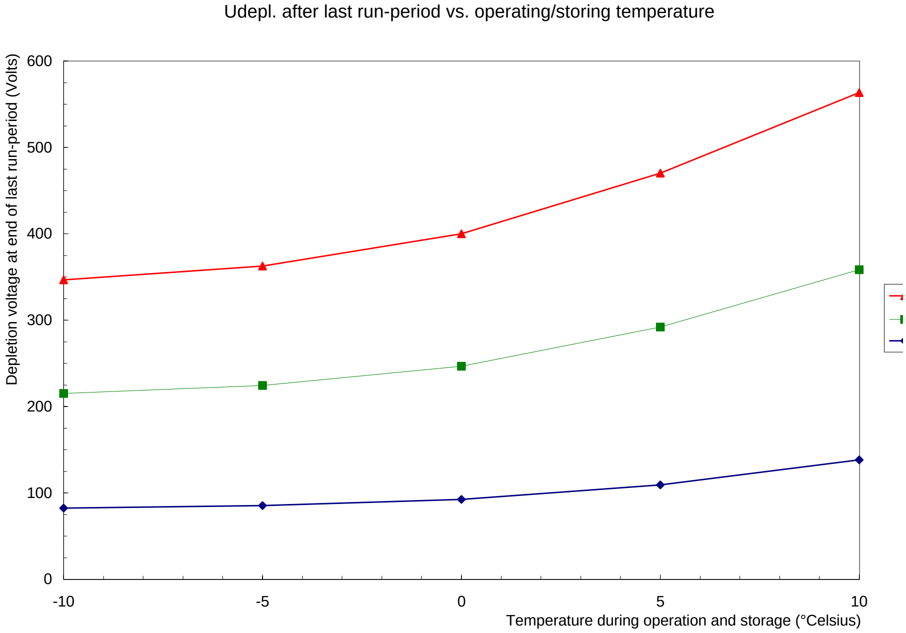

Figure H.18 Dependence of V_D on operating temperature for several integrated fluence values, assuming an annual warm-up period of 2 days at 20 °C, and 14 days at 17 °C. The detector thickness is assumed to be 300 µm.

2) The depletion voltage is not a well controlled parameter. However, the measurements indicate operation voltages, at the end of ATLAS, with 300 µm thick detectors of ~250 volts for n-in-n and ~450 volts for p-in-n to have high efficiency at low radii.

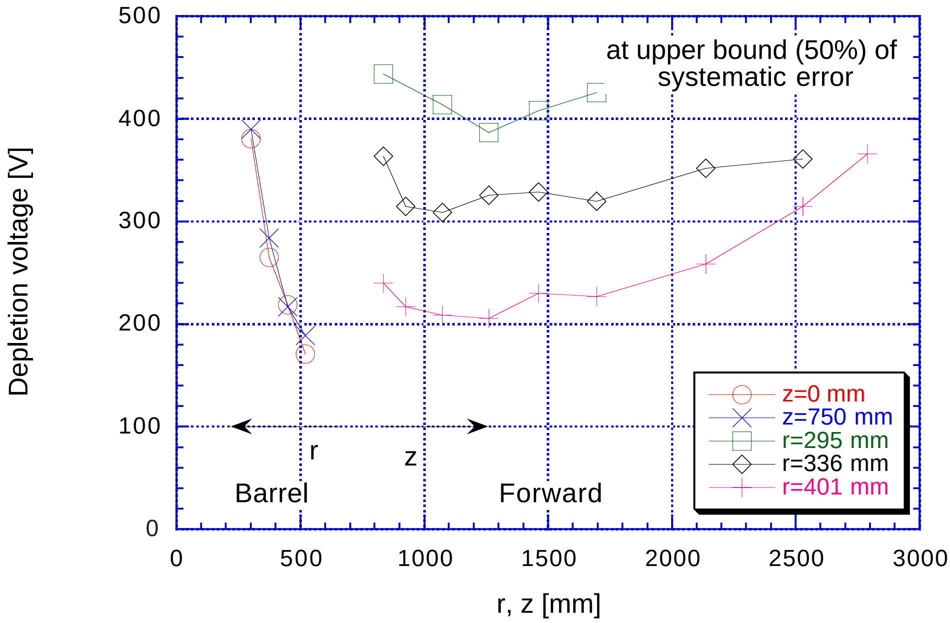

Figure H.19 Dependence of detector depletion voltage V_D as a function of detector position, assuming an integrated fluence after 10 years of 1.4 x 10^{14} n_{eq}/cm^2, and an operating temperature of -7 °C. The standard access procedure assumed for the SCT design is an annual warm-up of 2 days at 20 °C, and 14 days at 17 °C. The detector thickness is assumed to be 300 μm.

Table H.8 Expected depletion voltage V_D for each barrel module type, due to the expected fluence Φ at ATLAS. Also listed are results for a 50% larger fluence. The assumed access scenario is described in the text (SAP)

	V_D (volts)	V_D (volts) 1.5 x Φ	V_D (volts)	V_D (volts) 1.5 x Φ
	z=0 cm		z=75 cm	
Barrel 1	218	381	224	390
Barrel 2	150	265	161	284
Barrel 3	124	219	122	217
Barrel 4	95	171	106	189

3) The Hamamatsu n-in-n detector with polysilicon field plates above the p-stops has reached the stage of development that it could be ordered now with full confidence that it would perform well throughout the life of ATLAS at all SCT radii.

4) Commercial p-in-n detectors have not yet been fully measured. Noise measurements with electronics are missing for SINTEF p-in-n detectors, but from C-V measurements the rate of strip failures appears to be within the specification. Results are expected soon from Hamamatsu, CSEM, Micron and others.

Considering the other side of issue, resource and cost, two options were put for the decision,

1)Adopt p-in-n for the whole SCT with: (i) The voltage limited to < 350volts (ii)The innermost barrel and inner rings of detectors to be thinned to ~270microns if necessary to achieve full depletion. Projections for the SCT after 10 years of operation indicate, in the most pessimistic case, the depletion voltage, V_D, does not exceed 450V for 300 μm thick silicon; this means that even in

Table H.9 Expected maximum depletion voltage V_D for each disk module type, due to the expected fluence Φ at ATLAS. Also listed are results for a 50% larger fluence. The assumed access scenario is described in the text (SAP).

	V_D (volts)			V_D (volts) for 1.5 x Φ		
	Inner	**Middle**	**Outer**	**Inner**	**Middle**	**Outer**
Disk 1	255	208	136	444	364	240
Disk 2	-	179	122	-	315	217
Disk 3	238	176	118	414	309	209
Disk 4	222	186	116	387	326	206
Disk 5	234	188	130	408	329	230
Disk 6	245	183	128	426	320	227
Disk 7	-	201	147	-	352	259
Disk 8	-	206	179	-	361	315
Disk 9	-	-	210	-	-	366

Table H.10 Maximum expected detector leakage current I_L due to bulk damage, and minimum charge collection efficiency ε_{COLL} for detectors in each barrel, and each disk module type. In the case of (†), I_L is projected for an undepleted operating voltage of 300 V. The SAP access scenario is assumed.

	Max. bulk I_L per detector (μA)		Min ε_{COLL} (%)	
	Φ_{exp}	1.5 x Φ_{exp}	Φ_{exp}	1.5 x Φ_{exp}
Barrel 1	315	470†	92	79†
Barrel 2	250	375	92	90
Barrel 3	210	310	92	92
Barrel 4	190	280	92	92
Disk 1 Inner	315	470†	91	74†
Disk 1 Middle	280	420†	92	81†
Disk 9 Outer	285	425†	92	80†

the SAP scenario the operation at 350 V of *p*-in-*n* detector designs with the thickness of 270 µm will meet the LHC requirements.

2)Adopt n-in-n for the inner ring and inner barrel. For the outer layers the performance of 300 µm thick p-in-n detectors should be adequate.

The SCT community has chosen the first option.

H.4.6. Specifications

The tracker design requires one rectangular ‘barrel’ detector design and five slightly different designs for the wedge shaped ‘forward’ detectors which are to be built into disks. The dimensions of the individual barrel silicon wafers are 64 x 63.6mm^2, this being the largest usable area on a 4” wafer. The specifications discussed here are for barrel detectors but apply to all the designs except for the required geometrical differences.

In the specifications below, issues for the mask design are separated from the device properties (which give the device performance which each detector must fulfil) and the requirements, which are design goals which are necessary, but not testable on a device-by-device basis. The discussion on processing reflects current knowledge of how operational requirements in the severe radiation environment at the LHC may be met.

H.4.6.2 Detector mask specifications

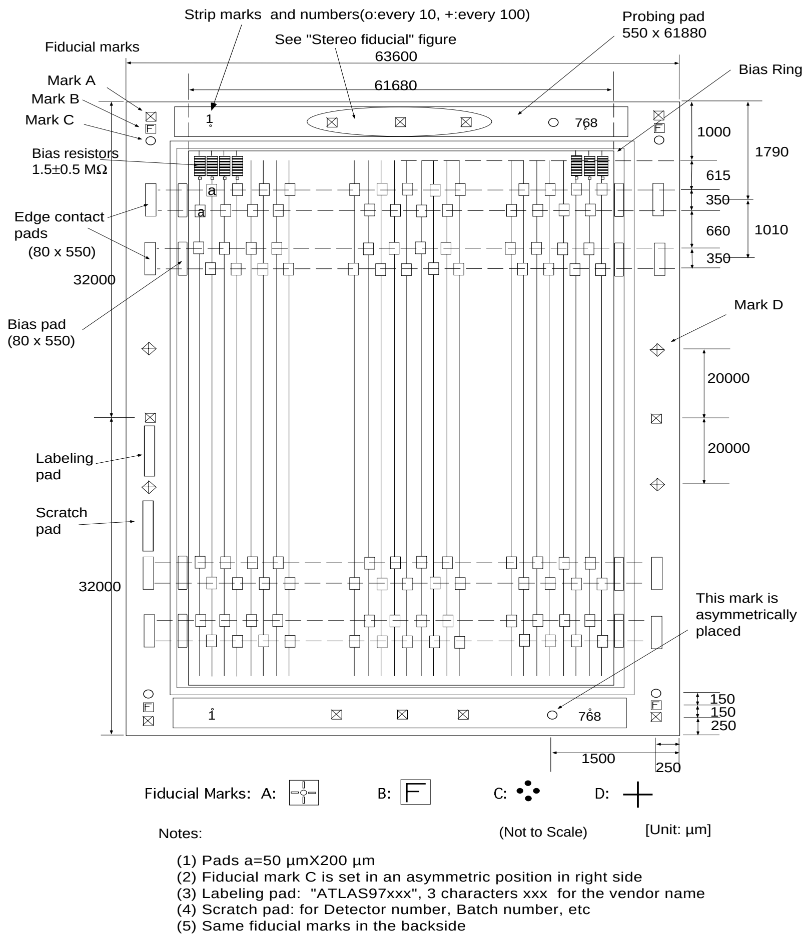

Figure H.20 Mask design and bond layout of the SCT Barrel Detector.

Figure H.20 shows, for a barrel detector, the overall device layout and locations of bias contacts, bond pads, alignment features, identification marks, etc.

- The barrel device size is 64 x 63.6 mm^2 cutting scribe line to cutting scribe line, with a sensitive region 62x61.6 mm^2. Optimisation is for 4” wafers.
- A total of 768+2 (768 read out) strips exist with implant strip dimensions 18µm wide, 62mm long, 80µm pitch, high doped *p*-implant.

- The readout strips are aluminium, capacitively coupled over the *p*-implant strips with a processed aluminium edge >1µm everywhere within the processed boundary of the implant strips. The capacitance and metal resistance requirements imply that these gaps should be as close to 1µm as mask alignment tolerances etc allow.
- The bias resistors overlap the implanted strips or are contained within the guard ring region.
- The distance between the sensitive region and the cut edge is 1mm.
- The distance between the outermost guard and the cut edge is > 500 µm.
- There are 200 x 56 μm^2 readout bond pads, in two rows, and daisy-chainable (see Figure H.20)
- The *p*-bias contacts are available at each corner (see Figure H.20).
- To enable strip evaluation probe points to readout strip implants exist at the contact point to the bias resistors.
- The detectors are passivated using silicon oxide.
- Every 10th strip is clearly numbered, with scratch pads used for detector labelling and alignment marks for module optical metrology (see Figure H.20).

H.4.6.3 Mechanical and optical specifications

The detector mechanical and optical specifications are described below:

- External cut dimensions are 64 x 63.6mm^2 with ±25 µm tolerance; edge chipping must be avoided.
- The thickness is 290 ±10 µm, with thickness uniformity ±10 µm.
- A mask alignment tolerance of < 3µm with respect to any other mask is required.

H.4.6.4 Detector electrical specifications

The detector electrical specifications are described below:

- The strip *p*-implant is <200 KΩ/cm.
- The aluminium readout strips satisfy a resistance of <20 Ω/cm.
- The bias resistance satisfies 1.5±0.5 MΩ polysilicon bias.
- $C_{coupling}$ > 10 pF/cm
- The depletion voltage (initial) is required to satisfy V_D< 100V.
- The total initial leakage including guard is required to be I_L< 6µA at 150V and I_L< 20µA at 200V. An increase in I_L by < 2µA after 24 hours in dry air is required to establish stability.
- The processing reproducibility is monitored on test structures (V_{FB}, t_{ox}, implant and polysilicon resistivity, aluminium sheet resistance, etching uniformity, dielectric strength etc). To check the dielectric integrity I_L < 1nA/cm^2 after 1 hour at 100V measured on large area test structures is required. This is needed to ensure adequate protection against `beam splashes' occurring when the detector is being operated at high voltage.

H.4.6.5 Bad strip quality specifications

Detectors may suffer bad strips because of defective strips, or from the polysilicon connection (the strip connection to bias via polysilicon broken).

- Each aluminium strip is to be contacted with a probe to check for no shorts through the coupling dielectric at 50V. Other defects may include metal/diode breaks or shorts to neighbours or broken polysilicon contact.
- A mean strip acceptance per detector of 99% in each delivery with no devices below 98% is required.

H.4.6.6 Detector performance and processing specifications

Each detector must satisfy the additional requirements listed below before and after irradiation at the corresponding maximum operating voltages. However, these criteria cannot be checked on a detector by detector basis.Therefore delivered prototypes of the same design and processing as the production delivery are required to satisfy these conditions.

- The maximum operating voltage is 150V initial, and 350 after the equivalent of ~2 x 10^{14} 24 GeV protons/cm^2
- It is required that $R_{inter\text{-}strip} > 2 \times R_{bias}$ at the maximum operating voltage.
- $C_{Total\text{-}Load} < 1.2$ pF/cm at maximum operating voltage.
- The strip current $I_L < 1\mu A$ per readout strip at -10 °C and 350V after the equivalent of 2 x 10^{14} protons/cm^2, and $I_L < 50$ nA at 150V prior to irradiation.
- The total current $I_L < 1$ mA at -10 °C and 350V after the equivalent of 2 x 10^{14} protons/cm^2.
- No excess noise due to micro-discharge [8-25] should exist at the maximum operating voltage. (this can only be checked after connection to electronics).
- After irradiation, the number of strips failing the pre-irradiation criteria should remain within the pre-irradiation acceptances.

The aim of these specifications is to safely satisfy the performance requirements; consequently the processing steps below are required (alternative solutions proven to 2×10^{14} protons/cm^2 will also be considered).

- The *p*-implant is > 10^{14} cm^{-2} and of 1-1.5μm implant depth.
- The strip capacitor dielectric is made from silicon oxide and silicon nitride layers.
- The back contact *n*-implant is of a level > 10^{14} cm^{-2}.
- The substrate doping is *n*-type with resistivity range 3 KΩcm < ρ < 8 KΩcm.
- The substrate oxygen concentration is typically 5 x 10^{15} cm^{-3} and < 10^{16} cm^{-3}.
- The substrate carbon concentrations is typically 5 x 10^{15} cm^{-3} and < 2 x 10^{16} cm^{-3}.

H.5 Readout Electronics

The front end electronics is based upon a one-bit digital (binary) readout architecture. This choice is supported by test-beam and bench prototype studies, and is the most cost-effective implementation meeting the performance requirements. Any strip which collects charge above an externally adjustable threshold fires a per strip discriminator.

The binary output is stored in a pipeline until an ATLAS trigger initiates readout for that beam crossing. General ATLAS design considerations have resulted in a deadtime-less readout, and this has forced simultaneous read-write operations on the front-end pipeline. A consequence for this architecture is significant data reduction in the front end chips, meaning that the discriminator performance, thresholds, noise, and pickup must be well controlled.

The beam bunch crossing rate of 40 MHz and the high luminosity result in expected occupancies in the SCT up to 0.6% every 25 ns caused by real tracks. In order to simplify track reconstruction, it is important to associate each hit to a specific beam crossing. The limit on noise hits has been set so as make them a negligible addition to the expected occupancy.

The combination of occupancy and crossing frequency also dictate the bandwidth needed to transmit the data off the detector. In order minimise material and cost, data compression is required on the detector and the readout architecture is event driven. That is, data is only transmitted off detector in response to a Level 1 Accept signal for a specific beam crossing. Data is held in on-detector buffers for the duration of the Level 1 latency (<2.5 μs) waiting for the decision to transmit the data or discard it. The readout speed is defined by the 100 kHz level-1 trigger rate, since the tracking data are used for level-2 trigger decisions.

H.5.7. Specification

The specification for the key parameters of the SCT readout electronics are listed in Table H.11 and discussed briefly below. The parameters discussed here apply mostly to the readout electronics as a system and have obvious implications for detailed specifications of all components.

Noise

The front end system must provide a sufficient signal-to-noise ratio to ensure a good efficiency and low noise occupancy. The equivalent noise charge (ENC) for the front-end system is defined including the silicon strip detector parameters. The ENC defined this way is substantially larger than the pure electronic requirement on a single front end channel.

Occupancy due to noise

The noise occupancy is required to be significantly less than the real hit occupancy to ensure that the noise hit rate does not affect the data transmission rate or track reconstruction. A noise occupancy of 5×10^{-4} requires that the discrimination level in the front end electronics is set to 3.3 times the rms noise.

Timing resolution

To minimize the data to be read out and to simplify tracking, unique crossing identification is required. The silicon charge collection time of 10 ns then mandates edge-sensing discriminators, with a maximum time walk of 16 ns for the nominal threshold setting and full range of input signals. The fraction of outputs shifted to the wrong beam crossing is required to be less than 1%.

Table H.11 Specifications for the SCT readout electronics.

Parameter	Specification
Noise	< 1500 e^-
Efficiency	99%
Occupancy due to noise	5×10^{-4}
Bunch crossing tag resolution	1 bunch crossing
Occupancy due to real hits captured in extra bunch crossing slots	1% of real hit occupancy
Double pulse resolution	50 ns for 3.5 fC signal following 3.5 fC signal
Large charge recovery time	1 µs for 3.5 fC signal following 80 fC signal
Maximum average L1 trigger rate	100 kHz
Minimum L1 trigger spacing	2 bunch crossings
Pipeline length	128 locations
Depth of de-randomizing buffer	8 locations
Voltage compliance	± 5% of nominal
Operating temperature	± 2.5 °C of nominal
Functionality temperature range	-15 °C to 30 °C
Power dissipation	< 3.8 mW / channel
Radiation total dose	2×10^{14} n / cm^2 10 Mrad

Double pulse resolution

In an edge sensing system, double pulse resolution affects efficiency. It is required to be 50 ns to ensure <1% data loss at the highest design occupancies.

Large charge recovery time

A low rate of events resulting in large charge deposition due to slow particles is expected. Therefore, although not very critical, it is desirable that the recovery time after large overloads is limited.

Trigger

The front end electronics operates at an average trigger rate of 100 kHz. The ATLAS requirement is for a 75 kHz trigger rate upgraded to 100 kHz, but because of its highly integrated nature, the full SCT electronics chain is designed for 100 kHz. The minimum spacing between consecutive triggers is 2 bunch crossings; statistical variations in trigger arrival beyond this must introduce <1% data losses for 1% occupancy. This drives the specification for the bandwidth of data links and the depth of the de-randomizing buffer.

Pipeline length

The pipeline length must correspond to the maximum trigger latency specified by the trigger system. With contingency, this is 3.2 µs which corresponds to 128 locations of the pipeline.

Voltage compliance

Significant voltage drops along the power distribution cables are incurred to reduce the amount of material in the sensitive area of the tracker. This requires the front end electronics to be insensitive to a bias voltage variation of ± 5% of the nominal values.

Temperature

The electronics must operate without re-calibration within ± 2.5 ˚C of its nominal value. In order to allow testing at room temperature it is required that overall readout system has full functionality in the temperature range between -15 ˚C and 30 ˚C.

Power consumption

The power consumption given in Table H.11 is the maximum permissible for the on-detector electronics. This is the number used in the design of the cooling system. The actual power consumption is estimated to be between 3.0 mW and 3.2 mW per channel, including the optical interface.

Radiation

The total radiation levels are specified separately for the displacement damage as a fluence of 1 MeV equivalent neutrons and for ionizing radiation as a dose absorbed in $Si0_2$.

H.5.8. System Design

The SCT readout electronics can be sub-divided into the following component systems: Front-end Electronics, Links, Cables, Power Supplies, Detector Control System (DCS) and Monitoring. The Off detector Readout and Control is not described here. Figure H.21 shows a schematic of the various electronic subsystems making up the SCT.

The front-end electronics include all the integrated circuits and other components that are mounted onto hybrid assemblies which become part of each detector module. These ICs perform the initial amplification of signals, discrimination, pipeline buffering, data compression and formatting the data for transmission. Diagnostic and test capability is provided in the front-end ICs (such as variable charge injection into the front-end pre-amps) but these are kept to a minimum to keep chip size and power to a minimum.

Data links transmit the data off detector. Other links transmit clock and control signals to the detector. The system is highly distributed with individual links going to each module. This multiplicity matches the necessary band-width with a highly parallel architecture to enhance the reliability of the SCT. Standard commercial links are not practical for this application, therefore the design employs 40 MHz links developed specifically for this application.

The cable system provides all power and DC control signals to (and from) the detector modules from power supplies located off the detector. Individual cable paths are provided for each detector module. Segmenting the power distribution to each module offers a more robust system in that any single failure will disable only a small fraction of the SCT. It allows silicon bias to be adjusted for variations in radiation dose and monitoring of currents and control of voltages to each module. Inside the detector volume, the cables are made of low mass aluminium on Kapton. Outside the detector they are of conventional twisted pair construction.

The off detector readout and control system is the interface between the SCT detector modules and the ATLAS Data Acquisition (DAQ) System and the ATLAS Trigger, Timing and Control (TTC) System. There are two main functional blocks; the Readout Driver (ROD) and the

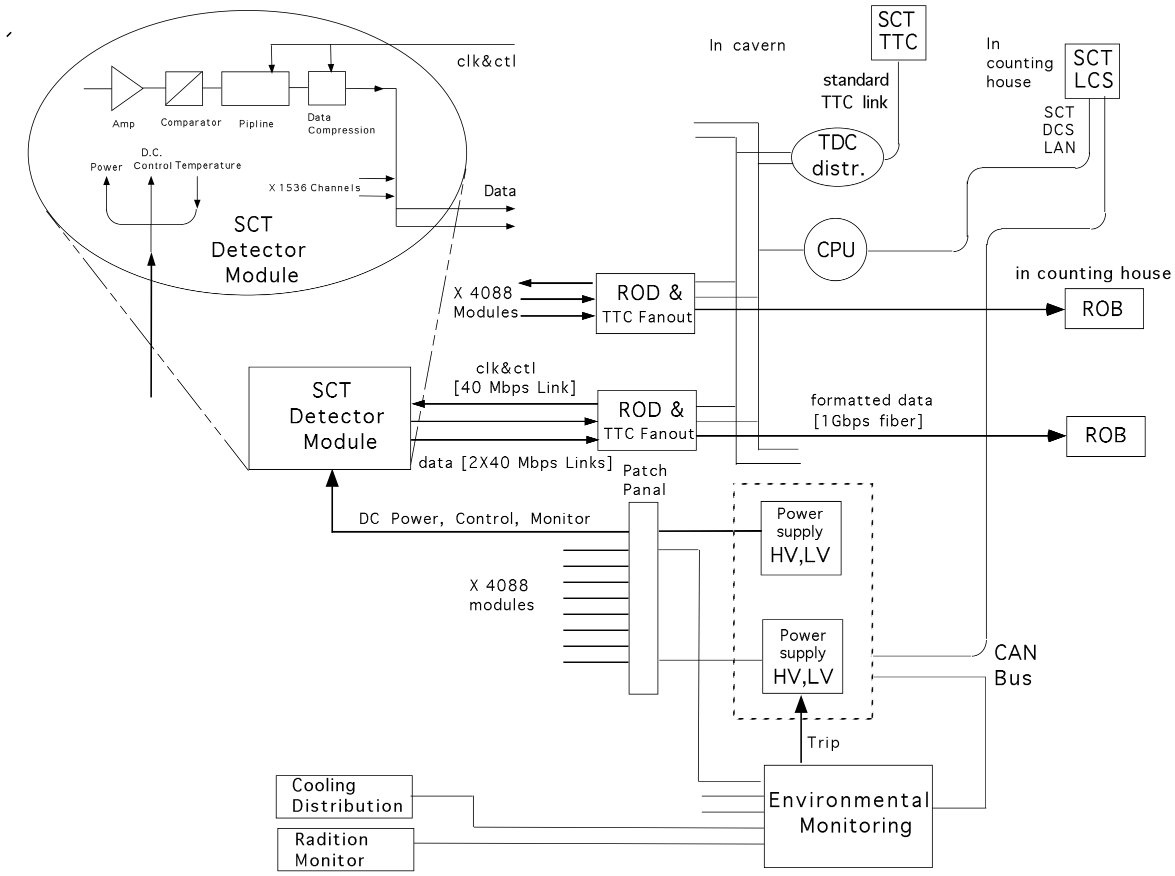

Figure H.21 Schematic of SCT Electronics sub-systems.

SCT-TTC distribution. The RODs receive data from the detector modules, interpret the SCT protocol, monitor for errors, reformat, buffer the data and feed it to the ATLAS standard Readout Buffers (ROB). The SCT-TTC interfaces to the ATLAS standard TTC. It receives clock and control information from the TTC, decodes the subset required, reformats and distributes it to the SCT-TTC links using the SCT protocol.

The power supplies provide all necessary power to the front-end, on-detector electronics and to bias the silicon detectors. This subsystem also includes a few necessary DC control signals required by the on-detector electronics. Each module has separate individual supply channels and current monitoring. This ensures a robust system and allows control of grounding.

The SCT-DCS is the interface between the SCT and the ATLAS general DCS. It interfaces the power supplies, the off detector readout and control system, the various monitoring systems, and the alignment and cooling systems to the centralized ATLAS control system. It also provides a means for locally controlling the SCT independent of the ATLAS DCS and will allow stand alone running of the SCT before integration into the complete ATLAS detector.

Monitoring functions in the SCT are widely dispersed, both in the physical distribution of the sensors and in the distribution of the initial destination of the information. Electrical performance of the detector modules is monitored via the power supplies measuring currents and voltages. The leakage current of each detector is also a good measure of temperature once it has been calibrated, but there is also one temperature probe (RTD) on each detector module. Additional temperature monitors accompany the cooling system inside and outside the detector volume. There are further temperature, humidity and pressure sensors associated with the alignment system. Separate radiation monitors monitor beam focusing problems. All of the monitoring systems feed data into the SCT-DCS.

Those monitors which track characteristics that may have an impact on the safety of the detector have separate hardware connections to trips which will protect against damage to the SCT.

H.5.9. Power Supplies

Power supplies for the SCT are segmented to provide self contained low and high voltage channel separately to each module. The power supply system also provides a set of control lines to the module. The voltages are:

- +3.5 V analog power for bipolar amplifier / discriminator circuits,
- +4.0 V digital power for CMOS pipeline circuits, DORIC3, a front-end clock and L1 distribution chip, and a dual LED driver circuit LDC,
- +10 V PIN photo-diode voltage for a diode connected to DORIC input,
- detector bias voltage, and
- low current control lines.

The power supply system has current, voltage and temperature monitoring features as well as over-current protection and safety systems.

The modularity of SCT power supplies follow the modularity of the detector so that 4088 power supplies serve the 2112 barrel and 1976 forward detector modules.

The required parameter values for the LV and HV power from each supply are summarised in Table H.12 . In addition to voltages listed, a bipolar preamplifier current control is required. The maximum current of this voltage is 6 mA per module (0.5 mA per chip).

Table H.12 Required parameters for the SCT power supplies.

Parameter	Analogue Voltage	Digital Voltage	PIN Voltage	Bias Voltage
Nominal value [V]	3.50 ± 5%	4.00 ± 5%	10.00±5%	10 - 300
Maximum current	900 mA	240 mA	10 μA	4 μA - 4 mA
Voltage setting resolution [V]	0.01	0.01	0.1	1.0
Current monitoring accuracy	1 mA	1 mA	1 μA	multi-range
Time for voltage adjustment	100 μs	100 μs	100 μs	20 ms
Start / stop ramping	unspecified	>2 V / s	unspecified	unspecified
Over-current trip at	1200 mA	350 mA	12μA	programmable
Over-voltage trip at	5.50 V	6.00 V	11.00V	400 V
Allowable ripple (peak to peak)	35 mV	35 mV	100 mV	200 mV

H.6 Modules

H.6.10. Description of module design

H.6.10.7 The barrel module

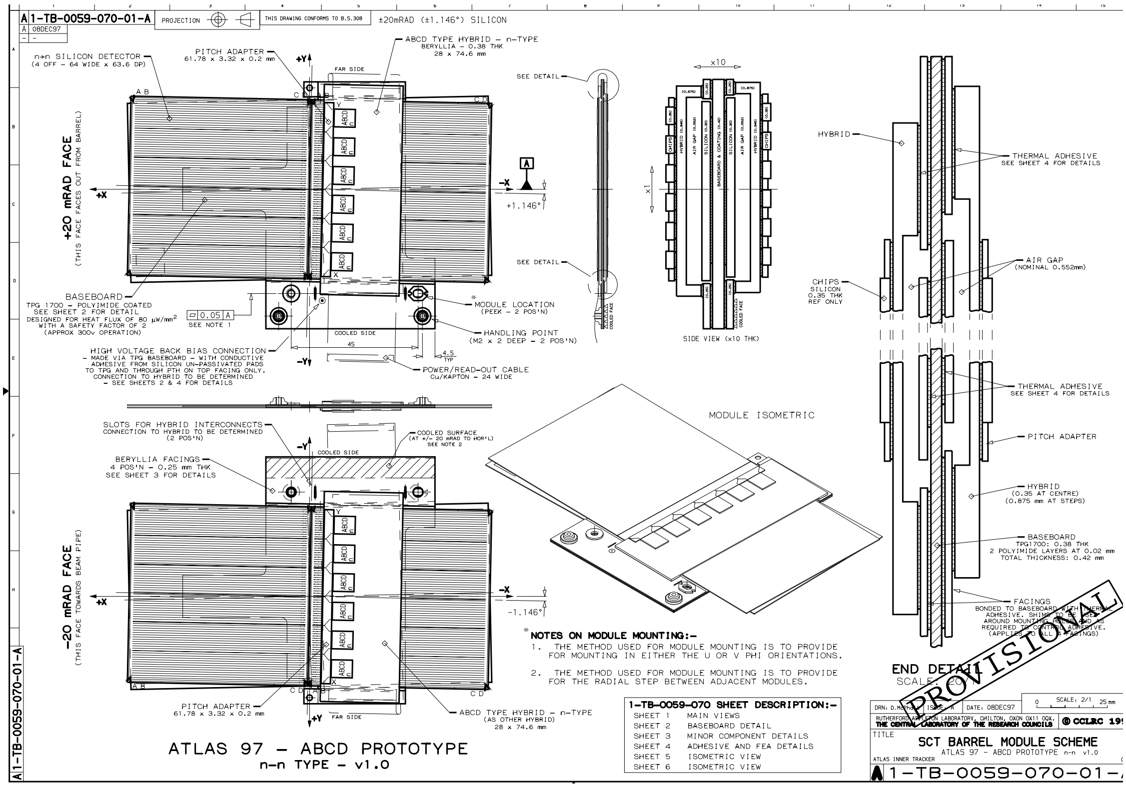

Figure H.22 Configuration of the barrel module.

In the barrel region, each layer consists of silicon strip modules of 4 single-sided silicon detectors with active area 61.6 x 62.0 mm^2, and geometric area 63.6 x 64.0 mm^2. Within the module, two detectors are daisy-chained for each side of a module. On one side 768 strips of 80 μm pitch and active length 123.2 mm are aligned precisely along the beam direction. The back-side detector pair is identical, but rotated by 40 mrad, to provide a z-measurement capability. One side of the module measures the r-ϕ coordinates (“axial strips”) while the other side measures the 40 mrad rotated coordinate (the “stereo strips”). The use of small-angle stereo rather than orthogonal strips is motivated by the need to reduce the number of ghost hits near a real track in high-multiplicity events. A second motivation is to retain an r-ϕ measurement capability in the case of detector inefficiencies.

The silicon detector signals will be read out by binary front-end electronics. This choice dictated the readout of individual strips (rather than charge division), and therefore the 80 μm pitch (giving a point resolution in ϕ of < 23 μm, and a space point resolution $<15 \oplus 12$ μm including alignment). Within the barrel region, all detectors have the same pitch, and all modules are identical.

Figure H.22 is a schematic of the barrel module showing the key features in the design. Figure H.23 shows an expanded view of all the components. The measuring planes, each formed of a pair of wafers, are glued to a pyrolytic graphite (TPG) heat spreader. The baseboard serves as a mechanical support for the wafers and increases the thermal conductivity in the plane of the module. The TPG, with a thermal conductivity of 1700 W/m/K, significantly increases the in-plane thermal conductivity of the module. As shown in the figure, the baseboard protrudes out symmetrically on both sides of the module. The exposed tabs are the points at which the readout hybrids attach to the module. The hybrids form mechanical bridges across the silicon, in a design that reduces the thermal coupling between the front end chips and the silicon without contacting the silicon surface. An effort has been made to avoid gluing to the active surface, given the uncertainties associated with long term ageing and radiation effects.

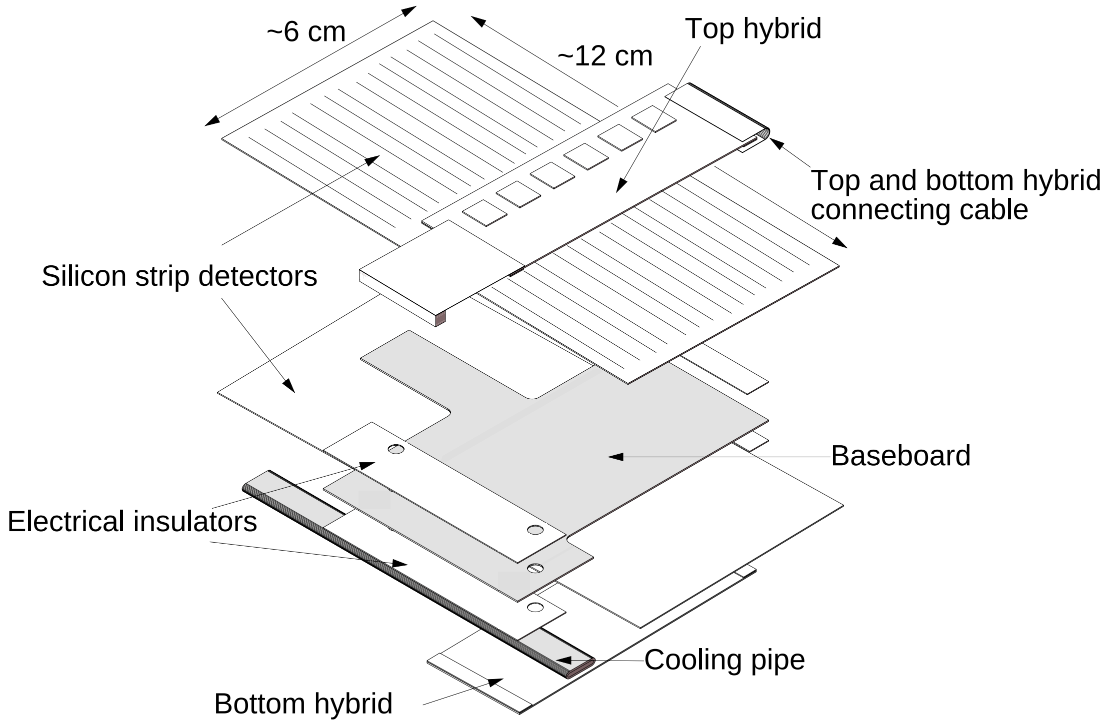

Figure H.23 Expanded view of barrel module.

The cooling contact to the barrel module is made at one side as indicated in the diagrams. The contact point includes dowel pin holes to accurately locate the module on the support structure.

In order to minimise the signal spread during operation in a 2 Tesla solenoidal field, the modules are mounted at an angle of 10° to the tangent. Modules are overlapped in a tile arrangement to minimise dead areas in the barrel region.

The module specifications are summarized in Table H.13 for the barrel.

Table H.13 Barrel module specification

Detector outer dimension	**63.6 mm x 128 mm**
Construction	Use four 63.6 mm x 64 mm *n*-on-*n* single sided detectors to form 128 mm long and back-to-back glued detectors
Mechanical tolerance	back-to-back: <5 µm (ϕ), <25 µm (r), <25 µm (z) Fixation point: <50 µm (ϕ), <100 µm (z)
Strip length	126 mm (2 mm dead in the middle)
Strip directions	Axial (along z-coordinate), U / V (40 mrad stereo)
Number of readout strips	768 per side, 1536 total
Strip pitch	80 µm
Hybrid	74.6 mm x 28 mm x 0.38 mm two single-sided hybrids bridged over the detector
Detector power consumption	1 W / total @ 0°C, (Heat flux / 300 µm) ~ 70 µW / mm^2
Hybrid power consumption	4.45 W
Operating temp. of detector	-7°C (average)
Uniformity of silicon temp.	<5°C
Permanent deformation	<5 µm (after 10 thermal cycles between -20 and +70°C)
Power on-off (Detector & Hybrid)	<10 µm
Dynamical deformation	<50 µm (between -10 and +30°C)

H.6.10.8 Mechanical tolerances

In the barrel, the strips on each of four detectors within a module should be relatively aligned to within ±5 µm in the ϕ direction and 25 µm in the z direction. The detector positions will be referenced to the overall support structure with dowel pins. The overall error in strip position is a combination of the error in placement of the rigid four detector unit with respect to the dowel pins and the error in placement of the module upon the support structure. The rigid four detector unit is to be placed within 50 µm in the r-ϕ direction and 100 µm in the z direction relative to the dowel reference frame but surveyed to 5 µm. The radial location of a wafer needs to be known to 50 µm upon the support structure. The thickness and shape of the individual modules should therefore vary by less than 25 µm. The skew of the detectors relative to the dowel pin reference frame is such that one end of a 12.6 cm strip is within 100 µm of the other end of the strip. In the forward modules the specifications are the same except that the z direction of the barrel module is replaced by the r direction.

H.6.10.9 The forward module

In the forward direction, the geometrical layout no longer allows the use of identical detector designs; nevertheless, the module construction is similar. Modules of daisy chained single-sided detector pairs with strip length ~12 cm and mean pitch ~80 µm, are arranged back-to-back with a 40 mrad stereo orientation.

Table H.14 Mechanical tolerances of the barrel module

	ϕ [μm]	r [μm]	z [μm]
Back-to-back pair	5	25	25
Strips to dowel pin	50	50	100
Stability	5	50	100
Module skew < 0.8 mrad			

Table H.15 Barrel module specification

Detector outer dimension	**63.6 mm x 128 mm**
Construction	Use four 63.6 mm x 64 mm *n*-on-*n* single sided detectors to form 128 mm long and back-to-back glued detectors
Mechanical tolerance	back-to-back: <5 μm (ϕ), <25 μm (r), <25 μm (z) Fixation point: <50 μm (ϕ), <100 μm (z)
Strip length	126 mm (2 mm dead in the middle)
Strip directions	Axial (along z-coordinate), U/V (40 mrad stereo)
Number of readout strips	768 per side, 1536 total
Strip pitch	80 μm
Hybrid	74.6 mm x 28 mm x 0.38 mm two single-sided hybrids bridged over the detector
Detector power consumption	1 W /total @ 0°C, (Heat flux/300 μm) ~ 70 μW/mm^2
Hybrid power consumption	4.45 W
Operating temp. of detector	-7°C (average)
Uniformity of silicon temp.	<5°C
Permanent deformation	<5 μm (after 10 thermal cycles between -20 and +70°C)
Power on-off (Detector & Hybrid)	<10 μm
Dynamical deformation	<50 μm (between -10 and +30°C)

There are 768+2 strips per measuring plane, with the first and last being used for field shaping and not connected to the readout. Each module subtends an angle larger than that required, to allow for a reasonable number of overlapping strips to ensure hermiticity and to facilitate module-to-module alignment using physics tracks. The nominal ϕ angle of a module is covered by strips 10 to 759. Figure H.24 shows a schematic of the wafer dimensions and relative positioning for each of the three module types used in the forward region. Each wheel is covered by one to three rings depending on its z position in the tracker.

The outer ring is covered by 52 modules and has an active strip length of 121.1 mm formed from two wafers butted end-to-end. The outer ring module subtends an angle of 7.117 degrees to allow for overlaps. The rotation point for the u/v stereo plane is at the intersection of the wafer break and the module centre-line.

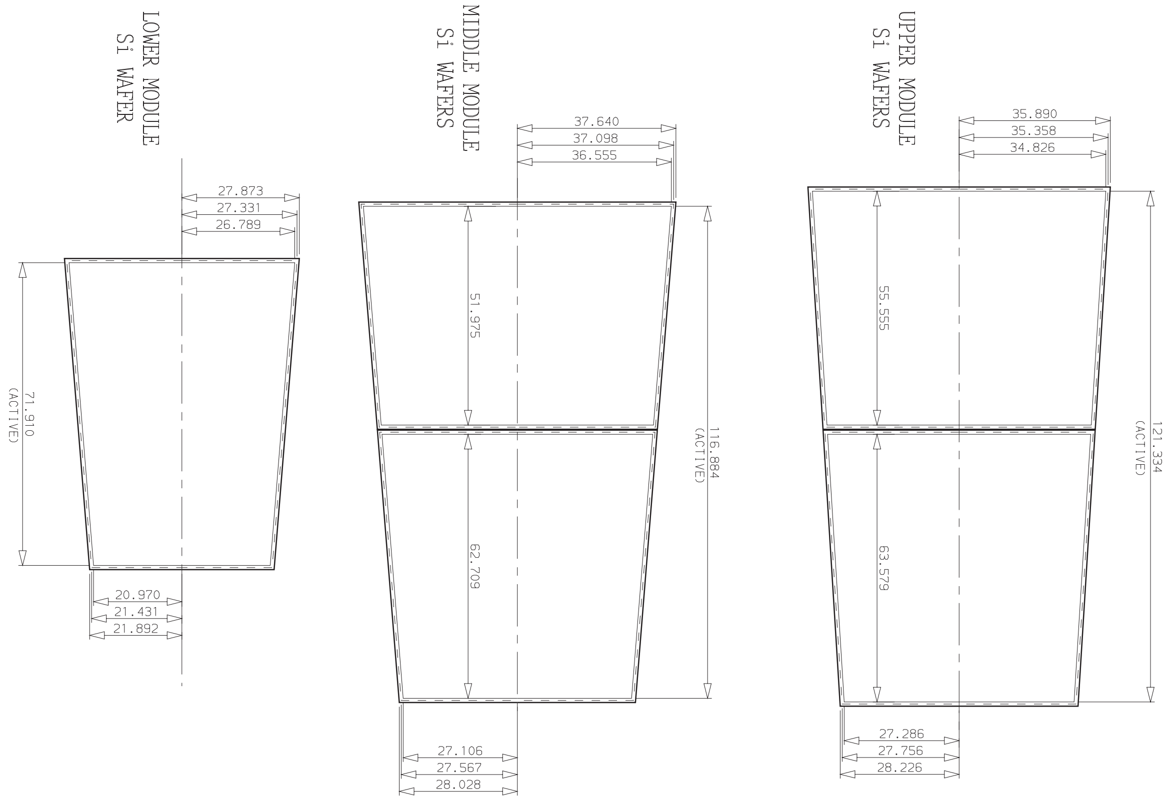

Figure H.24 Geometry of forward silicon detectors.

The middle ring, covered by 40 modules is, with the exception of those modules on wheel 8, also formed from two butt-joined wafers and has an active length of 116.7 mm. The middle ring modules on wheel 8 are formed from the upper wafer only and consequently have an active length of 52 mm. Middle ring modules subtend an angle of 9.252 degrees and the rotation point for the U/V plane is at the intersection of the wafer break and the module centre-line.

The inner ring is covered by 40 modules, each having an active strip length of 72 mm formed from a single wafer, subtending an angle of 9.252 degrees. The rotation point for the U/V plane is at the intersection of the mid-point of the active length of the wafer and the module centre-line.

Figure H.25 is a schematic of the forward middle ring module showing the key features in the design. Figure H.26 is an expanded view of the forward module. The two measuring planes, each formed of a pair of wafers, are sandwiched around a double sided readout hybrid and a central spine. The spine serves as a mechanical support for the wafers and increases the thermal conductivity along the length of the module. The same double sided hybrid is used for all modules and is formed on a support board into which two slots have been made. The slots act as a thermal break to prevent heat from the front-end electronics from entering into the silicon wafers. The electrical connections from the silicon strips to the readout electronics are made via fan-in structures mounted on either side of the hybrid bridging the thermal break.

The front-end electronics chip-sets are separated into two groups by the primary cooling contact which also serves as the module mounting point. Additional cooling may be provided by a contact to the far end of the spine. The additional cooling contact is used only for full length middle ring modules.

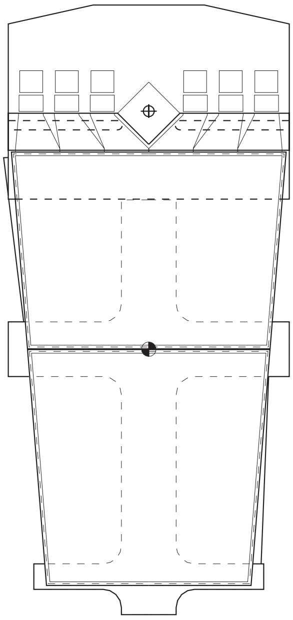

Figure H.25 Forward module layout.

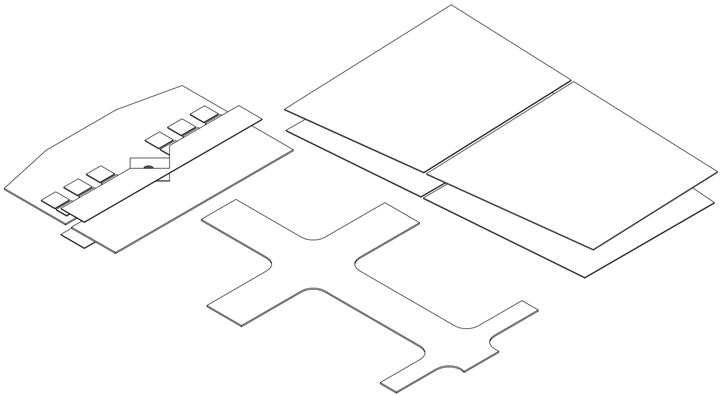

Figure H.26 Expanded view of a forward module.

The module specifications are summarized in Table H.16 for the forward modules.

H.6.10.10 Material

The material budgets for the barrel and forward modules are 1.20% and 1.28% of a radiation length respectively, when averaged over the full module area.

H.6.11. Critical design issues

The critical issue dictated the module design is the prevention of thermal runaway caused by the leakage current in the radiation-damaged detectors. The use of the heat spreader is optimized by finite element analyses.

Mechanical strength and thermo-mechanical distortions are other issues in the design. Use of materials with different coefficient of thermal expansion (CTE) must be compensated by using symmetrically. The modules must live in the thermal travel of +30 to -15 °C.

H.6.11.11 Thermal runaway finite element analysis of the barrel module

For the barrel module design (see Figure H.22), a finite element analysis of thermal simulation was performed [8-27]. The positive feedback of the temperature and the leakage current was taken account by changing the silicon resistivity as a function of temperature and the simulation was iterated till the temperature got stable or ran away. The temperature of the cooling contact was set at -10 °C. Figure H.27 shows the maximum temperature of the silicon detectors (T_{si} max) in the module as a function of the initial heat flux normalized at 0°C. The bulk heat flux after 10 years of operation at LHC is estimated to be 100 $\mu W/mm^2$ in the worst case. Figure H.28

Table H.16 Forward module specification

Detector outer dimension	**Outer: 56.5 - 71.8 mm x 123.1 mm** **Middle: 56.1 - 75.3 mm x 118.7 mm** **Inner: 43.8 - 55.8 mm x 73.9 mm**
Construction	Use four *n*-on-*n* single sided detectors to form back-to-back glued detectors (two detectors back-to-back in the inner ring)
Mechanical tolerance	back-to-back: <5 μm (ϕ), <20 μm(z), <25 μm (r) Fixation point: <50 μm (ϕ), <100 μm (r)
Strip length	Outer: 121.1 mm (2 mm dead near the middle) Middle: 116.7 mm (2 mm dead near the middle) Inner: 71.9 mm
Strip directions	Fan (along r-coordinate), U / V (40 mrad stereo)
Number of readout strips	768 / side, 1536 / total
Strip pitch	Outer: 70.8 - 90.3μm, Middle: 70.3 - 94.8 μm, Inner: 54.4 - 69.5 μm
Hybrid	76 mm x 52 mm x 0.5 mm one double-sided hybrid, set at the end of the module
Detector power consumption	1 W / total @ 0°°C, (Heat flux / 300 μm) ~ 70 μW / mm^2
Hybrid power consumption	4.45 W
Operating temp. of detector	-7°C (average)
Uniformity of silicon temp.	<5°C
Permanent deformation	<5 μm (after 10 thermal cycles between -20 and +70°C)
Power on-off (Detector & Hybrid)	<10 μm
Dynamical deformation	<50 μm (between -10 and +30°C)

shows the temperature profile in the module at the input heat flux of 160 μW / mm^2 for the model with a PG of the thermal conductivity of 700 W / m / K. The heat flux was the one where thermal runaway was about to start as seen in Figure H.27 . The module design against the thermal runaway is set to require the heat flux at the runaway point is twice away from the nominal heat flux in order to cope with the uncertainties, e.g., the variation of the cooling temperature, thermal conductivities in the finite element analysis. With the use of PG1700, which has the thermal conductivity of 1700 W / m / K, the barrel silicon strip module, thus, has the worst case safety factor of more than 2.

Expected Lifetime:

The thermal runaway has been expressed in terms of heat flux in the previous figures. In Figure H.29 , the lifetime of the detector has been expressed as a function of time, i.e., essentially the fluence, to understand directly the life of the detector [8-28]. The highest silicon temperatures were plotted in the figures. The runaway curves correspond to the curve of PG1700 in the Figure H.27 which runs away at the heat flux of 240 μW / mm^2. Since we are designing the module which should have the safety factor of 2, at least, the design runaway point as a function of time should be read one or more years shorter in the lifetime.

The thermal runaway is more drastic than in expressed in the heat flux. This is because the heat flux is the multiplication of voltage and current, and both are nearly the linear function of flu-

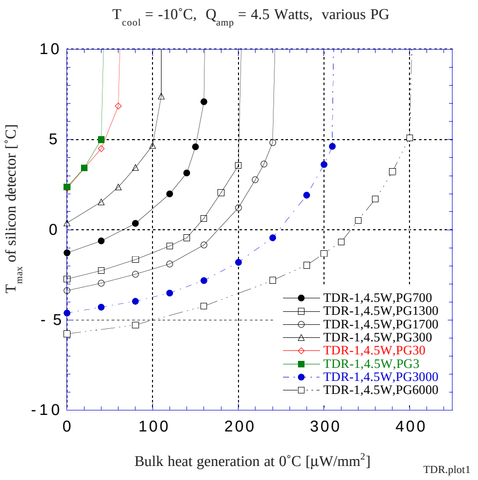

Figure H.27 Thermal runaway analysis as a function of heat flux in the silicon bulk for three thermal conductivities of PG. 100 µW/mm^2 is the heat flux at 300 V after 2 x 10^{14} pions/cm^2 fluence

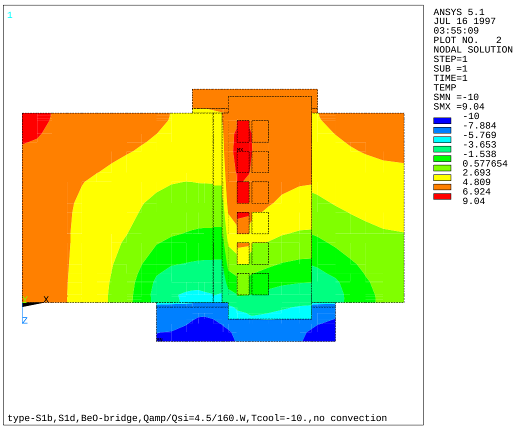

Figure H.28 Thermal profile finite element analysis with the input heat flux of 160 µW/mm^2 in the silicon and 4.5 W in FEE with the cooling contact at -10 °C

ence, i.e., the time, thus, being the heat flux as a quadratic function of time. The runaway is like quadratic as a function of heat flux near the runaway point. Thus, the total effect is that the thermal runaway is more or larger than a quadruple of time.

Thus, we expect the life of the detector to be 8 to 9 years in the worst case in the inner-most radius, if the bias voltage is applied along the increase of depletion voltage. The choice of the community is to limit the voltage to 300 to 350 V which, then, does not induce the thermal runaway situation as shown in the figure, but may lead to the loss of efficiency due to insufficient bias voltage to cope with the increase of depletion voltage. Although the inner-most layer may encounter trouble, the other 3 outer layers have more than 10 years of lifetime.

H.6.12. Module Prototypes

The concepts of current modules embody much information gained from a programme that has spanned a range of separate investigations. These have included studies of basic design components through to the construction of both partial and complete working modules.

H.6.12.12 Thermal profile measurement

Studies of temperature distributions and thermo-mechanical effects on prototype barrel modules have been carried out by a number of groups within the SCT. In general this work involved dummy modules fabricated with electrically inert but thermally and mechanically correct materials. An example of such a device is shown in Figure H.30 [8-29]. In this particular case, PG700 was used as a baseboard to provide very high thermal conductivity. A BeO ceramic plate was used as a dummy hybrid. An aluminium cooling pipe was attached to an extended lip of the base plate using a lubricant in order to achieve a good thermal contact between the base board and the aluminium pipe. Heaters were installed appropriately to simulate heat generation in the silicon detectors and front end readout chips.

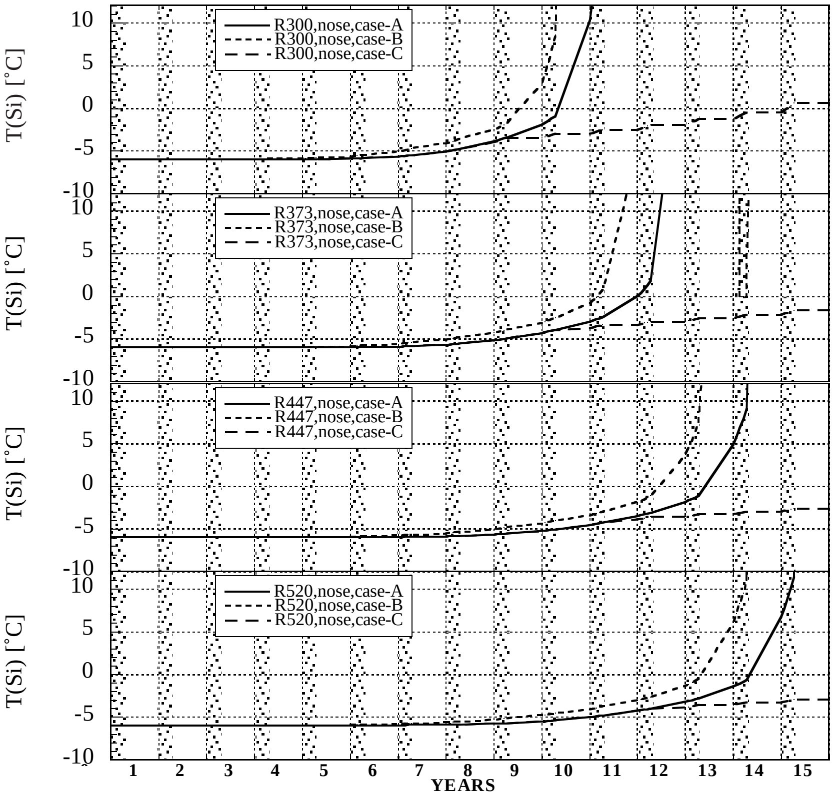

Figure H.29 Silicon temperature runaway as a function of time. The figures are for the radii of 300, 378, 447, and 520 mm from the top. “Case -A”: applying the bias voltage always 100 V above the depletion voltage, “Case-B”: applying the same bias voltage as the depletion voltage, and “Case-C” limiting the bias voltage up to 300 V. The runaway point corresponds to the heat flux of 240 µW/mm^2 with PG1700.

The test module was placed inside an environmental chamber. Both the ambient temperature inside the chamber and also the pressure were controlled in these measurements. The ambient temperatures was set to 0°C. The heaters were powered with 1 W for the silicon detectors and 3 W for the hybrid pair. The results are shown graphically in Figure H.31 . The data taken in vacuum were particularly useful in separating out the contribution of air convection cooling and to find parameters for use in finite element analyses. The observed results show temperature gradients across the module which are acceptable for use in the ATLAS SCT. These results are in good agreement with simulations and are confirmed in similar thermal modules also using PG heat spreaders, where the temperature difference between the coolant and the maximum hybrid temperature has been measured to be as low as 5.4°C [8-30].

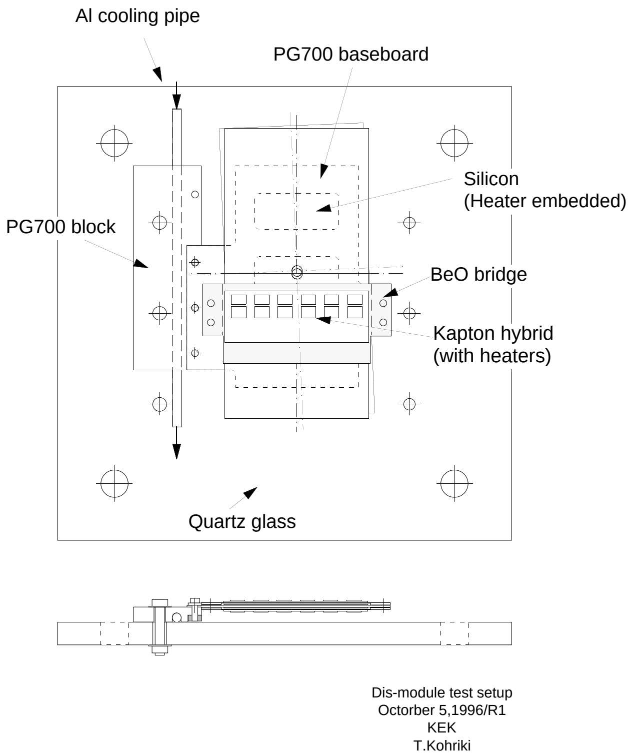

Figure H.30 Dummy barrel module and mounting used for thermo-mechanical studies.

H.6.12.13 Thermal runaway measurement

The process of thermal runaway has been demonstrated to take place in radiation damaged silicon detectors [8-31]. A silicon strip module was fabricated using two irradiated detectors. A mock hybrid, instrumented with a 3 W heater was placed near the middle of the module. A cooling pipe ran over the edge of the hybrid and the temperature of the furthest corner of the silicon was measured as a function of the bias voltage applied to the irradiated detectors. Heat was therefore generated in both the silicon and the hybrid. In this particular study stable thermal containment was obtained for all relevant bias voltages for cooling/air temperatures below 10º C, and runaway actually occurred at 250 V bias when they were increased to 20º C [8-32].

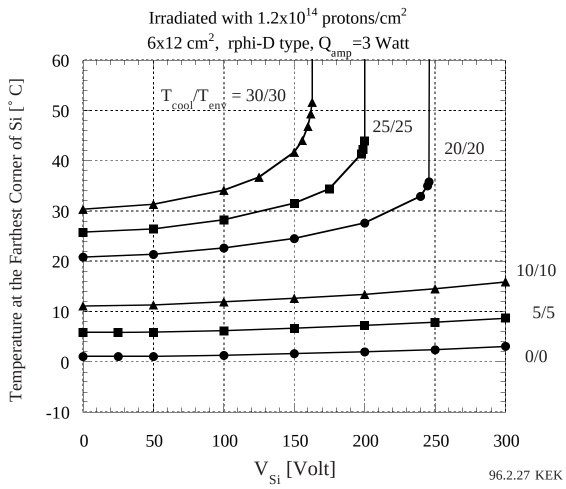

Figure H.32 Thermal runaway measurement in the module with irradiated detectors.

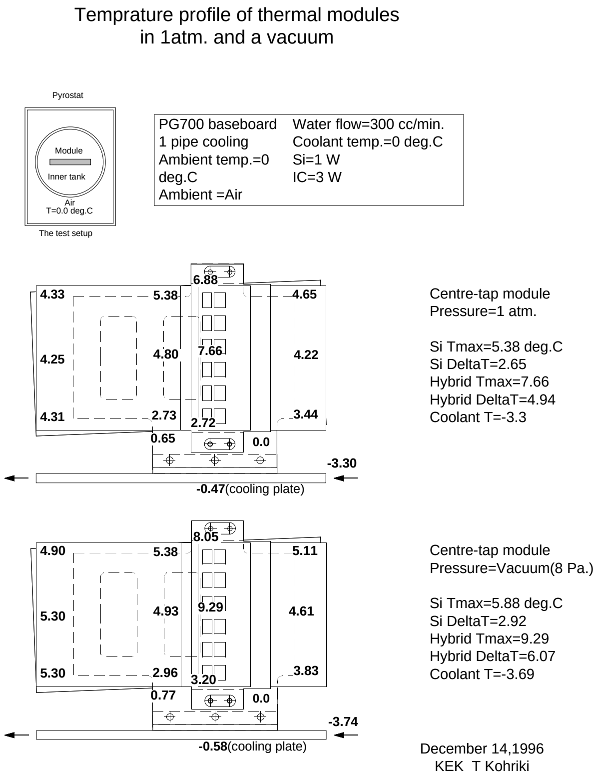

Figure H.31 Measured temperature distribution on test module containing PG heat spreader.

H.6.12.14 Thermo-distortion measurement

Another important thermo-mechanical issue concerns distortions between the construction temperature of ~25°C and the operating temperature of ~ -10°C. The thermal test barrel module (see Figure H.30) was measured using an ESPI system which is sensitive to distortions of 250 nm or larger. The module was mounted on a PG700 block which was rigidly attached on a pyrex glass plate of very small CTE and placed inside an environmental chamber to control the module and ambient temperatures, as shown in Figure H.33 . The distortion appeared as a fringe pattern of the ESPI measurement. An example is shown in Figure H.34 . This measurement was particularly sensitive to displacement near the perpendicular direction with respect to the module surface.

H.7 Support Structure

H.7.13. Specification

The final module alignment requirements are: .

Table H.17 Short term alignment requirements.

Barrel region	$\sigma_{r\text{-}\phi}$= 12µm	σ_r = 100µm	σ_z = 50µm
Forward region	$\sigma_{r\text{-}\phi}$= 12µm	σ_r = 50µm	σ_z = 200µm

These are basic constraints on the stability of the structure over a timescale which is sufficient to align the modules with the on-line alignment system and tracks.

H.7.13.15 Module placement

a) Overlaps and clearance

The minimum overlap (geometric overlap) between modules in the same layer is determined by the specification that the detector be hermetic to tracks with p_T > 1 GeV. An additional overlap is required to ensure that the build accuracy does not result in acceptance holes and that sufficient tracks pass through both layers for alignment purposes. To maintain the designed overlaps and clearances between modules on the same support, the following limits are placed on the sum of build error plus long term creep:

- To ensure that the r-ϕ overlap, which is important for alignment with tracks, is not significantly reduced from its design value, the maximum error is 100 µm in this direction;
- To ensure that the 500 µm overlap in the z direction in the barrel (r in forward) is not eliminated by the misplacement of modules it is required that the maximum error is 500 µm in this direction;
- Alternate modules are staggered by 2 mm in r in the barrel and 5 mm in z in the forward regions. This clearance must not be compromised, which implies an assembly accuracy of < 500 µm in the barrel and 1000 µm in forward direction;
- The positioning of whole barrels, of disks relative to each other, or of disks with respect to the nominal beamline can have errors in z of 2 mm before there is any significant effect on the geometric acceptance of the tracker.

b) Trigger

The planned use of tracking to provide a level 2 trigger threshold of a $p_T = 20\pm5$ GeV/c results in the need to calculate the absolute ϕ position of any strip to < 200 µm without using stereo information. A translation of the whole module in the r-ϕ direction can be corrected, but not a rotation, so the build plus creep for rotation must be less than 1.6 mrad within a 12 cm module and its mounting. Furthermore, the transformation from ϕ strip to ϕ value with 200 µm accuracy is only possible in the forward region if the disk is centred on the beam spot to within 500 µm.

H.7.13.16 Stability

The adopted philosophy is that the support structure is sufficiently stable that the final alignment constants, which must have the accuracies given in Table H.17 , can be derived from the initial survey combined with information from the on-line evaluation of track residuals and the FSI system. An initial alignment survey, repeated at a series of temperatures from -15°C to +25°C, will be used to cross calibrate the Frequency Scan Interferometry (FSI) network with module motions. The track alignment procedure is not yet precisely defined, but it is anticipated that high energy muon triggers, or tracks from minimum bias events, will be used. Since it is anticipated that the interval between fully understood three dimensional alignments will be a few weeks, the relative movement of modules on the same support should not exceed the final alignment tolerances in r and z during that period. It is noted that this should be relatively easy to achieve during stable running conditions, but not in the case of significant environmental changes.

The positions of the main support structures (barrels and disks) relative to each other can be measured more frequently with FSI and tracks. In the same time interval it is anticipated that tracks can be used to make small corrections to the alignment constants in the r-ϕ direction. This will bring a medium term r-ϕ error of each module in the global frame from <50 μm to the final r-ϕ error specification of <12 μm. The structure must remain stable to the full required alignment precision for this period.

The primary source of structural distortions are expected to result from localised temperature variations. By choosing low CTE carbon fibre construction these problems will be minimised. However, since the detectors, front-end electronics and cables dissipate up to 41 kW, some fraction of which depends on the nature of the data transmitted, small temperature changes are anticipated even during a fill.

H.7.13.17 Summary of specifications

Table H.18 summarises the tolerance specifications consistent with meeting the SCT alignment requirements. The quoted numbers are nominally rms units. In order to incorporate a safety margin, the numbers are used as engineering tolerances. The tolerances in Table H.18 are overall accuracies based on the physics performance required.

H.7.14. Support Structures

The choice of support structure for the SCT was motivated by the need to provide a stable structure having known and reproducible dimensional variations following repeated access over the detector lifetime, and following repeated temperature cycling in the range -15°C to +25°C. The chosen structure is the most cost-effective solution satisfying the specifications, and the choice is supported by design and prototype studies.

The central barrel region and the forward disk regions are mechanically isolated. The regions are suspended independently and are connected via a common final support rail fixed to the cryostat wall. As a result, there are three separate mechanical structures. Each of the assemblies has an outer enclosure, which acts as a gas volume and provides thermal insulation from the TRT.

Table H.18 Total Accuracy Requirements.

	Dimension	a (μm)	b (μm)	c (μm)	d (μm)
Build Accuracy	r-ϕ	250	50	500	50
	r	250	200	500	250
	z	1000	500	500	250
Maximum Long-term creep allowed, including effect of thermal cycling	r-ϕ	250	50	500	50
	r	250	50	500	500
	z	1000	500	500	250
Maximum motion between full track surveys (a few weeks)	r-ϕ		50		50
	r		50		100
	z		200		50
Stability under normal environment over a period of 2 days	r-ϕ	12	12	12	12
	r	50	50	100	100
	z	200	200	50	50

a/ Forward modules relative to the nominal beamline

b/ Forward modules relative to others on the same wheel

c/ Barrel modules relative to the nominal beamline

d/ Barrel modules relative to others on the same barrel

H.7.15. Barrel Structure

The support structure in the barrel region consists of four concentric carbon fibre cylinders. Each cylinder has two 0.2 mm thick skins of ultra-high modulus carbon fibre in a cyanate ester resin (CFRP). These are separated by a CFRP honeycomb of 6 mm thickness. The fibres are aligned to achieve a zero-CTE in the z and ϕ directions. The radial CTE is also low. The cylinder ends are terminated in a zero-CTE carbon fibre flange, which contributes significantly to the barrel rigidity. The cylinders are rigidly joined using a zero-CTE perforated end-plate, which connects to the end-flanges. The connection of the barrels via the end plates provides a further substantial improvement in the mechanical rigidity of the individual cylinders. The end plates are suspended from the inner TRT barrel via four interlink struts. The suspension is via a dynamic load equalisation scheme so that the structure remains unstressed; this has not yet been designed in detail.

Individual barrel detector modules are attached by precision fixations to a Barrel CFRP cylinder with precision brackets. A detail of the local support showing the cable layout, module brackets, and the cooling contact is shown in Figure H.38 .

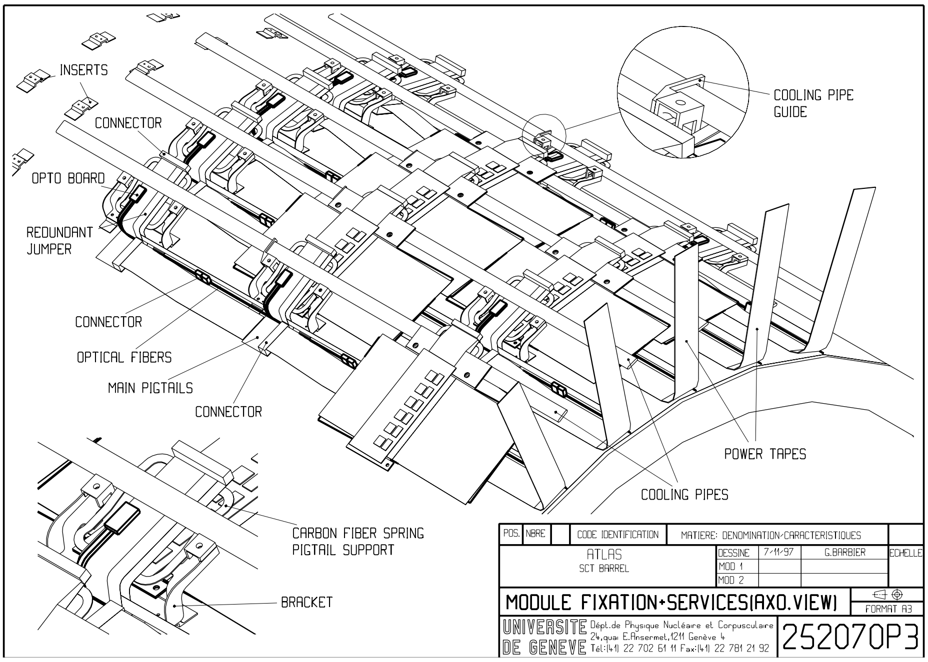

Figure H.38 Details of local support, showing module fixations, cable layout, and cooling pipes.

H.7.16. Cooling

The silicon detectors, front-end electronic hybrids, and cables must be cooled to control leakage current, radiation induced doping changes, and to remove heat generated by front end chips and DC voltage drops. Evaporative cooling using Fluorocarbon medium is foreseen since it cools by the liquid-gas phase transition and therefore offers near isothermal performance.

H.8 SCT Project Management

H.8.17. Participating Institutes

The following lists all physicists and senior engineers from institutes who have committed to the construction of the SemiConductor Tracker project.

University of Bergen, Department of Physics
Contact person: B. Stugu

Laboratory for High Energy Physics, University of Bern
Contact person: K. Pretzl

University of Birmingham
Contact person: J Dowell

Cavendish Laboratory, Cambridge
Contact person: J.R. Carter

CERN
Contact person: P. Weilhammer

Institute of Nuclear Physics, Cracow
Contact person: P. Malecki

Faculty of Physics & Nuclear Techniques (FPNT), University of Mining & Metallurgy, Cracow
Contact person: W. Dabrowski

Fakultaet fuer Physik, Albert-Ludwigs-Universitaet, Freiburg
Contact person: J. Ludwig

DPNC, University of Geneva
Contact person: A. Clark

University of Glasgow
Contact person: K. Smith

Department of Physics, Hiroshima University
T. Ohsugi, Y. Iwata
Contact person: T. Ohsugi

KEK
T. Haruyama, H. Iwasaki, T. Kohriki, T. Kondo, S. Terada, Y. Unno
Contact person: Y. Unno

Kyoto University of Education
R. Takashima
Contact person: R. Takashima

University of California, Irvine (UCI)
Contact person: A.J. Lankford

Lancaster University
Contact person: P Ratoff

LBL
Contact person: M. Gilchriese

University of Liverpool
Contact person: J. Jackson

Jozef Stefan Institute and Department of Physics, University of Ljubljana, Ljubljana
Contact person: M. Mikuz

Department of Physics and Astronomy, The University of Manchester
Contact person: M. Ibbotson

School of Physics, The University of Melbourne
Contact person: G. Taylor

Moscow State University Nuclear Physics Institute
Contact person: S. Basiladze

MPI
Contact person: V. Soergel

NIKHEF, National Institute for Nuclear Physics and High Energy Physics, Amsterdam
Contact person: B. van Eijk

University of Oslo
Contact person: S Stapnes

Physics Department, Oxford University
Contact person: R. Nickerson

Institute of Physics, Academy of Sciences of the Czech Republic, Prague
Contact person: J. Bohm

Czech Technical University, Prague
Contact person: S. Pospisil

Charles University, Prague
Contact person: I. Wilhelm

Institute for High Energy Physics, Moscow Region RU-128284 Protvino
Contact person: A. Vorobiev

Queen Mary & Westfield College (QMW), University of London
Contact person: A.A Carter

Rutherford Appleton Laboratory (RAL)
Contact person: M. Tyndel

University of California at Santa Cruz (UCSC)
Contact person: A. Seiden

Sheffield University
Contact person: C.M. Buttar

School of Physics, The University of Sydney
Contact person: L. Peak

University College (UCL), London
Contact person: T. W. Jones

University of Uppsala
Contact person: T. Ekelof

IFIC, Centro Mixto Universidad de Valencia -- CSIC
Contact person: J. Fuster

University of Wisconsin
Contact person: S. L. Wu

H.8.18. Organisation and Responsibilities

H.8.18.18 Design, development and common engineering

The organisation of the SCT project has evolved (and continues to evolve) to meet the needs of the project. The aim of the organisation is to co-ordinate and integrate the efforts of the participating institutes into a common project and to utilise the widely distributed expertise and effort. Initially the emphasis was on completing the required development, preparing the technical design and understanding the requirements and procedures for construction.

The following working groups are currently functioning. In each case the name of the current co-ordinator is followed by a list of institutes (or groups of institutes supported by the same funding agency) contributing:

Silicon detectors (P. Allport)

Australia, CERN, Germany, Japan, Norway, Russia, Switzerland, UK, USA, Valencia

Electronics (A. Grillo)

- FE ASICS (W Dabrowski)

  CERN, Cracow, Nikhef, Switzerland, UK, Uppsala, USA, Valencia

- Datalinks and Flex (A. Weideburg)

  Japan, Slovenia, Switzerland, UK

- Off-detector (A. Lankford)

  UK, Switzerland, USA

- Power Supplies & Cables (P. Malecki)

  Cracow, Prague, Slovenia, UK

- Control and Monitoring (R. Brenner)

  Russia, Uppsala

Modules (A. Carter, Y. Unno)

Australia, CERN, Cracow, Germany, Japan, Norway, Prague, Russia, Slovenia, Switzerland, UK, Uppsala, USA, Valencia

Engineering (E. Perrin, G. Tappern)

- Preparation for Module Construction (C Haber)

  Australia, CERN, Cracow, Germany, Japan, Norway, Prague, Russia, Slovenia, Switzerland, UK, Uppsala, USA, Valencia

- Barrel Structure and Assembly

  Japan, Switzerland, UK, Uppsala

- Forward Structure and Assembly

  Australia, Nikhef, Russia, Switzerland, UK

- Cooling

  CERN, Norway, UK

- Survey and Alignment (R. Nickerson)

  CERN, Nikhef, UK

Testbeam and Tracker Sector Prototype (S Stapnes)

Australia, CERN, Cracow, Germany, Japan, Nikhef, Norway, Prague, Russia, Slovenia, Switzerland, UK, Uppsala, USA, Valencia

Irradiation (C. Buttar, J. Carter)

CERN, Germany, Prague, Slovenia, UK, USA

H.8.18.19 Construction

Table H.19 provides an overview of the division of responsibilities agreed for the construction of the SCT. It summarises the contribution by funding agency, with entries showing the fraction of the project undertaken (in terms of the CORE cost estimate only for the material).

The basis of the work organisation is a ‘bottom-up’ approach to the construction of the SCT. It starts with the purchase of components (silicon detectors, FE ASICs etc), which after testing are built into modules. Modules are then assembled together with cables and datalinks into barrels and disks. The supply of cables, off-detector electronics, power supplies, cooling plant are organised as separate projects, as is the overall control and monitoring and alignment.

1. Silicon Detectors:

   The silicon detectors account for close to half of the total cost of the project. In general the institutes forming a cluster take responsibility for the purchase of the detectors for the modules they are constructing. In some cases, however, individual institutes concentrate their resources on areas in which they have particular interest and expertise. In this case, components such as detectors are, in some sense, exchanged for other components.

2. Frontend ASICs:

   As the testing of ASICs requires specialized equipment, this will be concentrated at 2 or 3 sites. The financial responsibility is shared between these institutes and the clusters assembling modules.

3. Module Assembly:

   A module is a unit consisting of four silicon detectors with FE electronics and is a fully functional component of the final detector. The construction and testing of modules will be carried out by 7 regional clusters. In general, clusters have chosen to assemble, test and supply modules for a particular part of the detector. The part of the detector and the number of modules required (including anticipated losses during assembly) are shown in Table H.20 .

   At this stage, the clusters are organizing the distribution of work within the cluster, and preparing the infrastructure required for module assembly. Further iterations on dividing work between clusters to better match resources and expertise is expected after approval. The responsibility of each cluster will be to deliver fully tested modules to the assembly sites.

Table H.19 SCT cost estimate of materials and sharing of responsibility

SCT Silicon Microstrip Detector Cost and Responsibility Summary

	Quantinty	Cost [MSFr]	Australia	CERN	Cracow	Czech	Germany	Japan	Nikhef	Norway	Russia	Slovenia	witzerland	UK	Uppsala	USA	Valencia
Detector:																	
- Barrel	10270	8.6						57%		18%				25%			
- Forward	8442	7.1					41%						29%	26%			7%
FEE ASIC's	63421	5.9		6%						3%			5%	26%	7%	50%	5%
FE comp.	1	0.4		25%						12%			19%		27%		19%
Digital circuts	1	1.2												100%			
Hybrids:																	
- Barrel/set	2516	2.1						27%						25%	18%	30%	
- Forward/set	2354	1.9		12%			30%		4%		4%		22%	27%			9%
Module comp.:																	
- Barrel/set	2223	1.1						27%		9%				25%	9%	30%	
- Forward/set	2080	1.1	5%				34%		5%				25%	27%			9%
Data link	4542	2.6		16%				18%		4%		8%		46%	4%		4%
Low-mass tape	4542	1.5					20%					44%	12%	25%			
Off-detector	4320	1.5												25%		75%	
Power supplies:		4.5															
- FE Low Vol	4320		31%			20%							29%	20%			
- Bias Vol.	4320			14%	20%		46%							20%			
- Cables	4188		31%	17%			24%						28%				
DCS	1	0.4													100%		
Structures:																	
Barrel	1	2.6		1%				25%		4%			40%	30%			
Forward	1	2.5	10%	1%					47%		4%			38%			
ID general:																	
- Cooling	1	0.8		25%						35%				40%			
- Alignment	1	0.9		25%					25%					50%			
Total		46.7															

Table H.20 List of institutions showing the planning for module construction.

Region of SCT	Num. of modules	Cluster	Institutes
Barrel 3	461	Nordic	Bergen, Oslo, Uppsala
Barrel 4	576+50	UK-B	Birmingham, Cambridge, Oxford, QMW, RAL
Barrel 5	691	Japan	Hiroshima, KEK, Kyoto Ed., Tokyo Met.
Barrel 6	756	USA	Irvine, LBL, UCSC
Forward - Disks 1,2,3	854	UK-V	Glasgow, Lancaster, Liverpool, Manchester, RAL, Sheffield, UCL, Valencia
Forward - Disks 4,5,6	~758	CS	Australia, CERN, Cracow, Geneva, Ljubljana, MSU, Prague
Forward - Disks 7,8,9	~758	CN	Freiburg, MPI, Nikhef, Prague, Protvino

4. Data-links and Flex cables

   These will be supplied by Japan, Slovenia, Switzerland and the UK in the proportions shown in Table H.19 .

5. Cables

   The supply of the custom-designed low-mass cables is primarily the responsibility of the Ljubljana group, with some contributions from other institutes.

   The financing of the standard cables is divided between most institutes as shown in Table H.19 .

6. Off-detector Electronics

   This will be the responsibility of Switzerland, UK, USA.

7. Power supplies

   Responsibility for the power supplies is divided in such a way that one group takes the lead responsibility with additional contributions from other institutes (Prague (low voltage) and Cracow (detector bias)).

8. Cooling

   Responsibility shared between CERN, Norway and the UK. It is foreseen that this will be part of an integrated cooling system for the SCT and Pixel detectors.

9. Alignment

   Responsibility shared between CERN, Nikhef and the UK. Again it is foreseen that this will be part of an integrated system for the ID.

10. Assembly and Survey:

    The design of the SCT is highly modular to ease the problems of assembly and commissioning. Overall this is co-ordinated by the engineers and the project leader. Although details are still to be finalised, it will involve the following steps:

a. Barrel pre-Assembly & Survey

Support structures will be equipped with fixtures and fittings under the responsibility of Switzerland and Uppsala. Assembly of modules to barrels is the responsibility of Japan and the UK together with the clusters supplying the modules.

b. Forward pre-Assembly & Survey

Support structures will be equipped with fixtures and fittings under the responsibility of Australia, Nikhef and Russia. Assembly of modules to disks is the responsibility of Nikhef and the UK and the clusters supplying the modules.

c. Final Assembly, Commissioning and Integration into the ID

Preparation for this is still in the early stages. This work will be centred at CERN in a purpose-built clean room on the surface above the pit. It will involve all institutes and be co-ordinated by the SCT project leader and engineers working closely with the other ID sub-systems and the ATLAS technical co-ordination.

11. Testing, Integration and Commissioning:

A major issue in the construction of the SCT is the scale of the project and how to prototype and guarantee the functionality of the full system. The strategy adopted is to benefit from the modularity of the SCT and, as time progresses, assemble and test increasingly large parts of the SCT. The following steps are planned:

a. Module-0

The first modules are constructed from the pre-production delivery of final components. A small number of modules will be built by each cluster and fully evaluated not only for performance, but also for uniformity between clusters.

b. TSP (Tracker Sector Prototype)

The first Module-0s will be built into 4 planes, as part of the overall TSP. This will give experience with the simultaneous operation and readout of ~ 20 modules. The performance of the complete tracking system - TRT, SCT and Pixels can be compared with simulation.

c. (Partially) equipped Disk

The first forward modules will be brought together as soon as possible to (partially) equip a first disk. Again this will be used for system tests and long-term tests.

d. (Partially) equipped Barrel

In order to have a large scale system test, a prototype cylinder will be (partially) equipped and brought into operation as soon as possible to gain experience.

All of these tests are sufficiently complex, that they will be run as individual projects, with well defined goals. The success of these initiatives will rely on contributions from the whole collaboration.

H.8.19. Schedules and Milestones

The construction schedule is determined by

- Completion of technical design and prototyping

  The technical design and all prototyping is expected to be finished this year (1998), or be sufficiently advanced to allow the start of tendering for the critical items (silicon detectors and FE ASICs).

  If possible, the production orders will be placed with a phased delivery. A pre-production batch, to be delivered as soon as possible for construction of Module-0, will be followed by a period for evaluation. Depending on the outcome, either small modifications will be required or production can continue over the following 2-4 years.

- Start of Physics

  For ATLAS to be ready for physics in mid 2005, the construction, assembly and testing of the SCT needs to be complete by the end of 2002. The following 2 years are scheduled for the integration and commissioning of the Inner Detector, first on the surface and then in-situ.

Figure H.39 shows the planned construction schedule. The prototyping currently underway is not indicated. For each line, there are 2 or 3 phases shown. Pre-production is the phase when the first “final” components are assembled into Module-0. This is then followed by production as explained above. In some cases (e.g. readout, power, cooling) some fraction of the items are required during assembly for testing and the production of these items is shown separately.

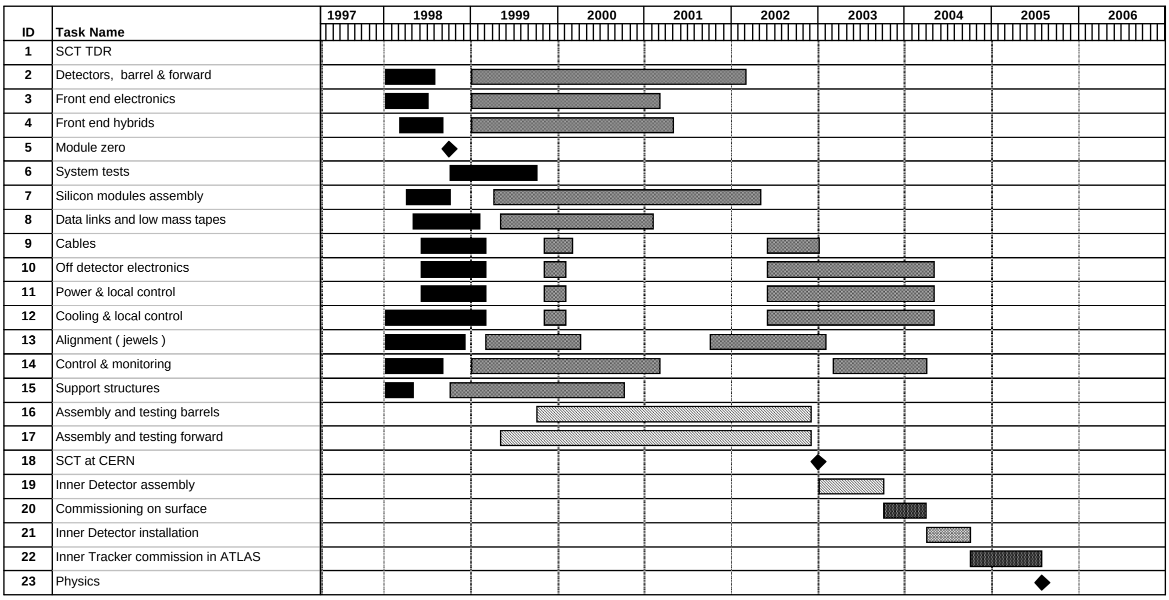

Figure H.39 Construction Schedule showing pre-production followed by construction.

Key Milestones are

- April 1997 TDR
- December 1997 Final design reviews and tender for detectors and ASICS
- September 1998 Freeze support structure design
- October 1998 Module-0
- January 1999 Start ASIC, Detector production
- July 1999 System tests (TSP; local supports, proto-barrels and disks)
- March 2001 Complete ASIC production
- March 2002 Complete detector production
- January 2003 SCT at CERN
- September 2003 Assemble ID

H.8.20. References

8-21 PYTHIA 5.7, T. Sjostrand, CERN preprint CERN-TH7111/93 and CERN-TH7112/93

8-22 F.W. Bopp et al., Phys. Rev. D49 (1994) 3236.
P. Aurenche et al., Phys. Rev. D45 (1992) 92.

8-23 P.J. Griffin, private communication.
This evaluation uses the ENDF/B-VI revision 4 cross-sections, and the methodology of P.J. Griffin et al., SNA RML Recommended Dosimetry Cross Sections, Sandia National Laboratories Report SAND92-0094.
See also:
A. Vasilescu, “The NIEL scaling hypothesis applied to neutron spectra of irradiation facilities and in the ATLAS and CMS SCT”, ROSE Collaboration Technical Note ROSE/TN/97-2 (Febuary 1997).

8-24 E. Fretwurst et al., Reverse annealing of the effective purity concentration and long-term operational scenario for silicon detectors in future Collider experiments, Nucl. Instr. Methods A342 (1994), 119.
A. Chilingarov et al., Radiation Studies and Operational Projections in the ATLAS Inner Tracker, Nucl. Instr. Methods A360 (1995) 432-437.
H.-J. Ziock et al., Temperature dependence of the radiation induced change of depletion voltage in silicon PIN detectors, Nucl. Instr. Methods A342 (1994) 96-104

8-25 T. Ohsugi et al., Micro-discharge at strip edge of silicon microstrip sensors, Nucl. Instr. Methods A383 (1996), 116-123.

8-26 I. Kipnis, Noise Analysis due to Strip Resistance in the ATLAS SCT Silicon Strip Module, LBLN Note 39307, August 1996.

8-27 T. Kondo, Thermal Simulation of the barrel SCT module-I and II, Oct, 97, ATLAS-INDET-No-201, 202

8-28 T. Kondo, Yearly operation profile of the ATLAS SCT modules, Jan. 98, ATLAS-INDET-No-203

8-29 T. Kohriki et al., Thermal profile measurement of the centre-tap and the end-tap modules, Nov. 96

8-30 G. Barbier et al., Status Report on Module Cooling and Mechanics, ATLAS Note ATLAS-INDET-NO-166 (1997).

8-31 T. Kohriki et al., First Observation of Thermal Runaway in the Radiation Damaged Silicon Detector, IEEE Trans. Nucl. Sci. 43 (1996) 1200-1202.
T. Kondo et al., ATLAS presentation ATLAS-SCT-TR-021 (March 1996).

8-32 T. Kohriki et al., Measurement of thermal runaway in the ATLAS SCT silicon strip module with irradiated detectors, Mar., 96